The decay of orbital angular momentum entanglement in atmospheric turbulence

F Stef Roux

International Workshop on

Singularities and Topological Structures of Light

Abdus Salam International Centre for Theoretical Physics

Trieste, Italy

8 – 12 July 2013

Contents

I. CLASSICAL SCINTILLATION

1. Turbulence and scintillation [1]

   Turbulence is a phenomenon found in fluids. The air in the atmosphere is an example of such a fluid. Turbulence causes random fluctuations in the refractive index of the fluid. On the other hand, scintillation is what happens to light propagating through a turbulent fluid. It is caused by the phase modulations induced by the random fluctuations in the refractive index, together with the subsequent diffraction. Refractive index fluctuations vary as a function of both time and space — the refractive index is a random three-dimensional function that gradually changes with time.

2. Refractive index fluctuations

   The fluctuations of the refractive index in a turbulent atmosphere are very small compared to the average refractive index of the atmosphere, and can be written as

   $$n(\mathbf{x}) = n_0 + \delta n(\mathbf{x}), \tag{1}$$

   where $\mathbf{x}$ is the position vector in three-dimensional space, n_0 is the average refractive index, which is approximately equal to 1, and the fluctuations in the refractive index is denoted by $\delta n(\mathbf{x})$. These fluctuations are much smaller than the average refractive index.

3. Scintillation: phase modulation + diffraction

   Although the primary effect of turbulence on the traversing optical beam is a pure phase modulation, after some subsequent propagation, the diffraction induced by the random phase modulations causes fluctuations in the intensity of the beam, which can for instance be observed as the twinkling of stars in the night sky. This combined effect is the scintillation process. The random phase modulation is done continuously along the propagation path — hence, an accumulated effect. Together with the diffraction of the beam, the random phase modulation progressively aggravates the distortion of the beam with increasing propagation distance. Figure 1 shows what a Gaussian beam looks like after it suffered severe scintillation.

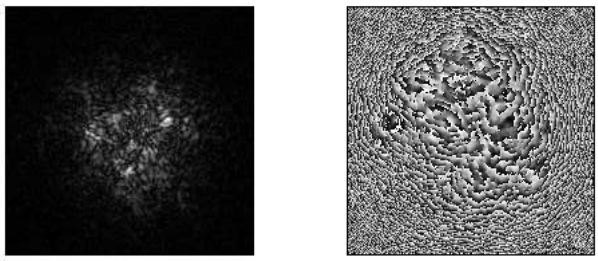

FIG. 1: Example of the intensity and phase of a distorted optical beam due to scintillation.

4. Weak/strong turbulence vs weak/strong scintillation

   Strong turbulence implies that the fluctuations in the refractive index are relatively large. However, strong turbulence does not necessarily imply strong scintillation. The amount of scintillation that an optical beam experiences depends on various parameters, including the strength of the turbulence and the distance of propagation. Scintillation increases with distance of propagation and it increases more rapidly in strong turbulence. Scintillation can still be weak even if the turbulence is strong, provided that the light propagated for only a short distance. The opposite is also true. If the turbulence is weak the scintillation of the beam can be strong if it propagated far enough.

5. Experiment to measure scintillation

To measure scintillation one can use the experimental setup that is shown diagrammatically in Fig. 2. Two beams are sent parallel to each other through the turbulent medium, separated by a distance Δx. The interference between the beams after they passed through the turbulence gives an indication of the strength of the scintillation.

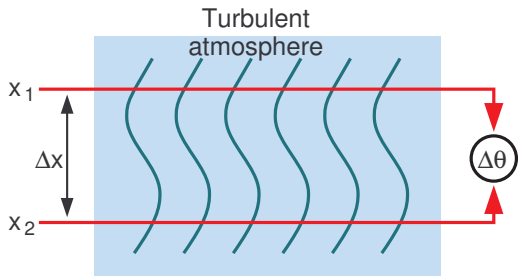

FIG. 2: Experimental setup to measure scintillation.

6. Phase structure function and phase autocorrelation function

The ensemble average of the interference between the two beams in Fig. 2 gives the phase structure function

$$D_\theta(d) = \langle[\theta(x_1, y_1) - \theta(x_2, y_2)]^2\rangle, \tag{2}$$

where $\langle\cdot\rangle$ is the ensemble average, D_θ is the phase structure function and

$$d = \sqrt{(x_2 - x_1)^2 + (y_2 - y_1)^2}. \tag{3}$$

For a homogeneous isotropic medium the structure function depends on only the distance d between the two points (x_1, y_1) and (x_2, y_2).

The phase structure function is related to the phase autocorrelation function

$$D_\theta(d) = 2R_\theta(0) - 2R_\theta(d), \tag{4}$$

where the phase autocorrelation function is given by

$$R_\theta(d) = \langle\theta(x_1, y_1)\theta(x_2, y_2)\rangle. \tag{5}$$

7. Phase from refractive index

The accumulated phase in the experiment in Fig. 2 is given by

$$\theta(x, y) = kn_0 z + k\int_0^z \delta n(\mathbf{x})\ \mathrm{d}z, \tag{6}$$

where $k = 2\pi/\lambda$ is the wavenumber. The first term gives an unimportant overall constant phase, which can be ignored.

8. Refractive index structure function and refractive index autocorrelation function

The phase autocorrelation function can now be written as

$$R_\theta(d) = k^2\int_0^z\int_0^z \langle\delta n(\mathbf{x}_1)\delta n(\mathbf{x}_2)\rangle\ \mathrm{d}z_1\ \mathrm{d}z_2. \tag{7}$$

The integrand is the refractive index autocorrelation function

$$R_n(r) = \langle\delta n(\mathbf{x}_1)\delta n(\mathbf{x}_2)\rangle, \tag{8}$$

where $r = |\mathbf{x}_1 - \mathbf{x}_2|$. The refractive index structure function is again related to the refractive index autocorrelation function

$$D_n(r) = 2R_n(0) - 2R_n(r), \tag{9}$$

where

$$D_n(r) = \langle |\delta n(\mathbf{x}_1) - \delta n(\mathbf{x}_2)|^2 \rangle. \tag{10}$$

Note that the refractive index structure function and refractive index autocorrelation function are three-dimensional functions whereas the phase structure function and phase autocorrelation function are two-dimensional functions.

9. Kolmogorov refractive index structure function

   Based on the Kolmogorov theory of turbulence [1], the refractive index structure function is given by

$$D_n(r) = \langle |\delta n(\mathbf{x}_1) - \delta n(\mathbf{x}_2)|^2 \rangle = C_n^2 r^{2/3}, \tag{11}$$

   where C_n^2 is the refractive index structure constant with units of $\mathrm{m}^{-2/3}$. The Kolmogorov theory is only valid in the inertial range, between an inner scale and an outer scale. The strength of the turbulence is determined by C_n^2, with values ranging from about 10^{-17} $\mathrm{m}^{-3/2}$ for weak turbulence to about 10^{-13} $\mathrm{m}^{-3/2}$ for strong turbulence.

10. Wiener-Khintchin

    It is often more convenient to work in the spatial Fourier domain. According to the Wiener-Khintchin theorem [2], the Fourier transform of the autocorrelation function gives the power spectral density function. Treating the autocorrelation function as a function of three spatial coordinates, one obtains a three-dimensional power spectral density

$$\Phi_n(\mathbf{k}) = \frac{1}{(2\pi)^3} \int R_n(\mathbf{x}) \exp(i\mathbf{k} \cdot \mathbf{x}) \, \mathrm{d}^3 x. \tag{12}$$

    However, in a homogeneous isotropic medium the power spectral density only depends on the magnitude of $\mathbf{k}$. Hence, $\Phi_n(|\mathbf{k}|)$.

11. Kolmogorov power spectral density

    The power spectral density for the Kolmogorov theory is given by

$$\Phi(|\mathbf{k}|) = 0.033 \, C_n^2 |\mathbf{k}|^{-11/3}. \tag{13}$$

    This is a sharply peaked function, shown in Fig. 3, and is singular at the origin.

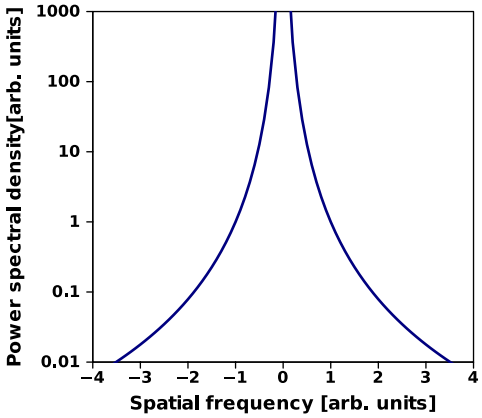

FIG. 3: Shape of the Kolmogorov power spectral density function.

12. Quantifying weak/strong scintillation

    As mentioned above, the strength of scintillation is not only determined by the strength of the turbulence, but also by the other relevant dimension parameters, namely the distance that the light is propagating through the turbulence z and the wavelength of the light λ. These parameters are combined into the Rytov variance [1], given by

$$\sigma_R^2 = 1.23 C_n^2 k^{7/6} z^{11/6}, \tag{14}$$

where k is the wave number ($2\pi/\lambda$). For plane waves, strong scintillation conditions exist when $\sigma_R^2 > 1$ and for a Gaussian beam (with radius w_0), strong scintillation exists when [1]

$$\sigma_R^2 > \left(t + \frac{1}{t}\right)^{5/6} \tag{15}$$

where we defined a normalized propagation distance

$$t = \frac{z}{z_R}, \tag{16}$$

with z_R being the Rayleigh range given by $\pi w_0^2/\lambda$.

II. QUANTUM ENTANGLEMENT

1. Entanglement

   A key aspect of quantum systems that is often exploited in quantum information technology is the property of quantum entanglement. This is a nonlocal correlation that can exist in multi-partite quantum states (quantum states for multiple subsystems, such as different particles). The role of entanglement was dramatically demonstrated in the EPR experiments [3], which show a violation of Bell's inequality [4].

   Considering the pure quantum state of a pair of photons, we say that this quantum state is entangle if is not separable, which means that one cannot factor it into a tensor product of states for the individual photons. For instance,

$$|\psi\rangle = \frac{1}{\sqrt{2}}\left(|1\rangle_A|0\rangle_B - |0\rangle_A|1\rangle_B\right) \neq |\mathcal{A}\rangle_A|\mathcal{B}\rangle_B. \tag{17}$$

   For mixed states the requirement of separability is generalized to become a sum of factorizable density matrices.

2. Concurrence

   In general it is challenging to compute the amount of entanglement in an arbitrary mixed multi-partite quantum state of arbitrary dimension. However, for a pair of qubits there exists a quantity called the concurrence that can be computed fairly easily [5, 6], even if the quantum state is mixed.

   The concurrence is given by

$$\mathcal{C}(\rho) = \max\left\{0, \sqrt{\lambda_1} - \sqrt{\lambda_2} - \sqrt{\lambda_3} - \sqrt{\lambda_4}\right\}, \tag{18}$$

   where λ_i are the eigenvalues, in decreasing order, of the Hermitian matrix

$$R = \rho(\sigma_y \otimes \sigma_y)\rho^*(\sigma_y \otimes \sigma_y), \tag{19}$$

   with ρ being the density matrix, * representing the complex conjugate and σ_y being the Pauli y-matrix, given by

$$\sigma_y = \begin{bmatrix} 0 & -i \\ i & 0 \end{bmatrix}. \tag{20}$$

3. Bell states

   The Bell states are the maximally entangled bipartite qubit states given by

$$\left|\Phi_{01}^{\pm}\right\rangle = \frac{1}{\sqrt{2}}\left(|0,0\rangle \pm |1,1\rangle\right) \tag{21}$$

$$\left|\Psi_{01}^{\pm}\right\rangle = \frac{1}{\sqrt{2}}\left(|0,1\rangle \pm |1,0\rangle\right). \tag{22}$$

III. SINGLE PHASE SCREEN APPROXIMATION

1. Paterson model

The problem of the decay of entanglement due to atmospheric scintillation has been considered from a conventional optics point of view, by, in particular, Paterson [7]. He made the assumption that one can represent the effect of turbulence on an optical field propagating through it, by a single phase screen, as demonstrated in Fig. 4. This assumption is valid provided that the scintillation remains weak over the entire propagation distance.

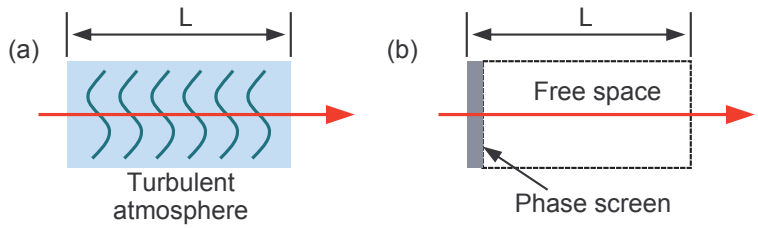

FIG. 4: Single phase screen approximation. In (a) the optical beam propagates through a turbulent medium for a distance L and in (b) that distance is replaced by a single phase screen and a free-space propagation of distance L.

Paterson's model is currently used as the basis for most work [8–11] that is being done on the decay of entanglement for photons propagating through atmospheric turbulence. Although it is not directly formulated in terms of quantum information theory [12], one can argue that Paterson's model represents a valid quantum process — it can be expressed as an operator product expansion.

2. Quantum operation for a single phase screen

Under weak scintillation conditions, one can assume that the turbulent atmosphere can be represented by a single phase modulation. The corresponding quantum process is a single step process

$$\rho(z) = U\rho(0)U^\dagger, \tag{23}$$

where the unitary operator is represented by a single phase factor $U \sim \exp[i\theta(x,y)]$.

Assuming that the original input density matrix is a pure state $\rho(0) = |\psi\rangle\langle\psi|$, one can express the individual output density matrix elements by

$$\rho_{mn}(z) = \langle m|U|\psi\rangle\langle\psi|U^\dagger|n\rangle, \tag{24}$$

where $|m\rangle$ represents a discrete orthogonal basis for the transverse mode, such as the Laguerre-Gaussian modes. We insert an identity operator, resolved in terms of the two-dimensional spatial modes to obtain

$$\langle m|U|\psi\rangle = \int \langle m|\mathbf{r}\rangle\langle\mathbf{r}|U|\psi\rangle \ \mathrm{d}^2r \tag{25}$$

$$\langle\psi|U^\dagger|n\rangle = \int \langle\psi|U^\dagger|\mathbf{r}\rangle\langle\mathbf{r}|n\rangle \ \mathrm{d}^2r, \tag{26}$$

where $\mathbf{r}$ is the two-dimensional transverse position vector. The mode functions for the transverse spatial modes are given by $E_n(\mathbf{r}) = \langle\mathbf{r}|n\rangle$ and the single phase screen approximation leads to $\langle\mathbf{r}|U|\psi\rangle = \exp[i\theta(\mathbf{r})]\psi(\mathbf{r})$, where $\psi(\mathbf{r}) = \langle\mathbf{r}|\psi\rangle$ is the input field and $\theta(\mathbf{r})$ is the phase function that is obtained from the refractive index fluctuations δn by an integration along the direction of propagation as given in Eq. (6).

The expression for the density matrix element in Eq. (24) then becomes

$$\rho_{mn}(z) = \iint E_m^*(\mathbf{r}_1)E_n(\mathbf{r}_2)\psi(\mathbf{r}_1)\psi^*(\mathbf{r}_2)\exp\left[i\theta(\mathbf{r}_1) - i\theta(\mathbf{r}_2)\right] \ \mathrm{d}^2r_1 \ \mathrm{d}^2r_2. \tag{27}$$

3. Ensemble average of the density matrix

The unitary operator U in Eq. (24) represents the result of a particular instance of the refractive index fluctuations. Since we do not presume to have knowledge of the medium at any particular time and therefore can only

make statistical predictions about its effect, we need to compute the ensemble average over all refractive index fluctuations. The density matrix elements are therefore given by

$$\rho(z) = \left\langle U\rho(0)U^\dagger \right\rangle = \sum_s^N \frac{1}{N}\, U_s\rho(0)U_s^\dagger, \tag{28}$$

where the subscript s denotes a particular instance of the refractive index fluctuations. When the ensemble average is applied to the expression in Eq. (27), it only affects the exponential function containing the random phase modulations and leads to

$$\langle \exp\left[i\theta(\mathbf{r}_1) - i\theta(\mathbf{r}_2)\right]\rangle = \exp\left[-\frac{1}{2}D_\theta\left(|\mathbf{r}_1 - \mathbf{r}_2|\right)\right], \tag{29}$$

where $D_\theta(\cdot)$ is the phase structure function. For Kolmogorov turbulence it can be expressed as

$$D_\theta(x) = 6.88\left(\frac{x}{r_0}\right)^{5/3}, \tag{30}$$

in terms of the Fried parameter [13]

$$r_0 = 0.185\left(\frac{\lambda^2}{C_n^2 z}\right)^{3/5}. \tag{31}$$

The ensemble average of the density matrix element is therefore given by

$$\langle \rho_{mn}(z)\rangle = \iint E_m^*(\mathbf{r}_1)E_n(\mathbf{r}_2)\psi(\mathbf{r}_1)\psi^*(\mathbf{r}_1)\exp\left[-\frac{D\left(|\Delta\mathbf{r}|\right)}{2}\right]\, \mathrm{d}^2r_1\, \mathrm{d}^2r_2. \tag{32}$$

One can turn the integration in Eq. (32) into a dimensionless integral by normalizing $\mathbf{r}_1$ and $\mathbf{r}_2$ by some dimension parameter, such as the beam radius w_0. The resulting expression that follows from the integral thus only depends on the dimensionless combination w_0/r_0. All the adjustable dimension parameters are contained in w_0/r_0, including the propagation distance z. As a result the complete z-dependence is determined by the w_0/r_0-dependence, which sits inside the structure function $D(\cdot)$. The dimensionless combination w_0/r_0 quantifies the strength of scintillation.

4. Quadratic structure function approximation

The integral in Eq. (32) is not analytically tractable due to the power of 5/3 that appears in the structure function, inside the exponential function. Often this problem is avoided by approximating the structure function in Eq. (30) by a quadratic structure function

$$D \sim \left(\frac{x}{r_0}\right)^{5/3} \rightarrow \left(\frac{x}{r_0}\right)^2. \tag{33}$$

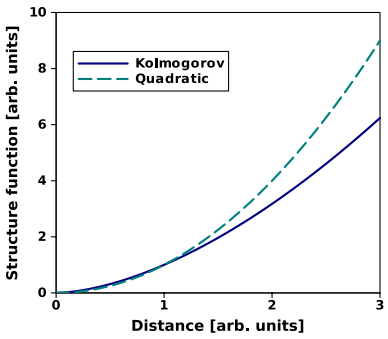

FIG. 5: Comparison of the Kolmogorov structure function with the quadratic structure function.

In Fig. 5 the shape of the quadratic structure function is compared with that of the Kolmogorov structure function.

5. Classical singular optics in turbulence

   Much work has been done on optical vortices in turbulence in the context of classical light. Some notable examples are the following. David Fried identified [14] the effect of 'hidden phase' in adaptive optics systems; Gbur and Tyson [15] performed numerical simulations to study the conservation of topological charge in atmospheric turbulence; Dipankar, *et al.* [16] studied the trajectories of optical vortices in atmospheric turbulence; numerical simulation were also performed by Voitsekhovich, *et al.* [17] and Rao [18] to study how the number of vortices evolve during propagation through turbulence. Tyler and Boyd [19] performed a calculation of the power coupled into neigbouring OAM modes during propagation through turbulence, under the single phase screen approximation.

6. OAM entangled quantum states in turbulence

   Most of the work on the decay of OAM entanglement in turbulence is based on the Paterson model. Gopaul and Andrews [9] computed the probability to detect the photons of OAM entangled quantum states after passing through turbulence, using the Paterson model. Jha, *et al.* [11] showed that one can measure the concurrence directly in the case where qubits are encoded in a plane waves basis. They used the Paterson model to compute the decay in the concurrence for such qubits due to turbulence. On the other hand, Semenov and Vogel [10, 20] used a different model based on an attenuating system to study the effect of turbulence on quantum light in the limit of weak scintillation.

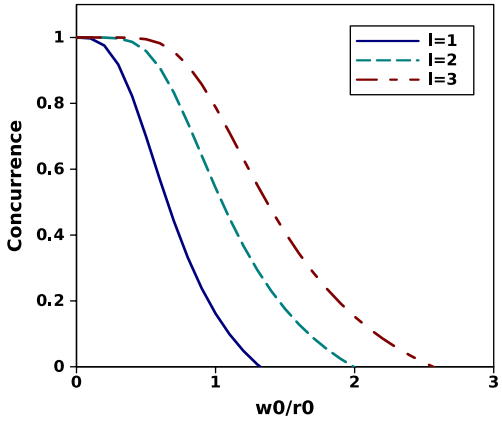

FIG. 6: Concurrence as a function of w_0/r_0 from the single phase screen calculation.

Smith and Raymer [8] used the Paterson model with the quadratic structure function approximation to calculate the concurrence as a function of w_0/r_0, for an initial state that is a Bell state in the OAM basis. They found that the concurrence tends to decay to zero when w_0/r_0 is on the order of 1, as shown in Fig. 6. The fact that the a nonzero concurrence only exists up to where $w_0/r_0 \approx 1$ indicates that entanglement only exists as longs as the scintillation is weak. However, the curves in Fig. 6 also indicate that for larger values of the azimuthal index the concurrence survives up to slightly larger values of w_0/r_0.

7. Regions of scintillation

   What are the conditions under which the single phase screen approximation is valid? Since the single phase screen approximation assumes that scintillation is weak, we need to consider the conditions for weak scintillation. For this purpose we use the Rytov variance σ_R^2, defined in Eq. (14). The diagram in Fig. 7 shows the different regions in terms of the Rytov variance as a function of the normalized propagation distance t. From Eq. (14) one notes that for any particular optical beam propagating through homogeneous turbulence, the value of σ_R^2 is proportional to $t^{11/6}$. Three such lines are shown in Fig. 7 for different turbulence strengths. One can see that these lines start off in the region of weak scintillation at the bottom of the diagram. Then they move up toward the region of strong scintillation as the beams propagate further. Eventually these lines cross the boundary into the region of strong scintillation, as given by Eq. (15). However, at the same time (for weak turbulence) or even before it (for strong turbulence) it also crosses the line where $\omega_0/r_0 = 1$ (dashed line in Fig. 7), which is approximately where the concurrence goes to zero. The dashed line is obtained by expressing the Rytov variance in terms of ω_0/r_0, given by

$$\sigma_R^2 = 1.637\, t^{5/6} \left(\frac{\omega_0}{r_0}\right)^{5/3}. \tag{34}$$

For $\omega_0/r_0 = 1$ we find that σ_R^2 is proportional to $t^{5/6}$.

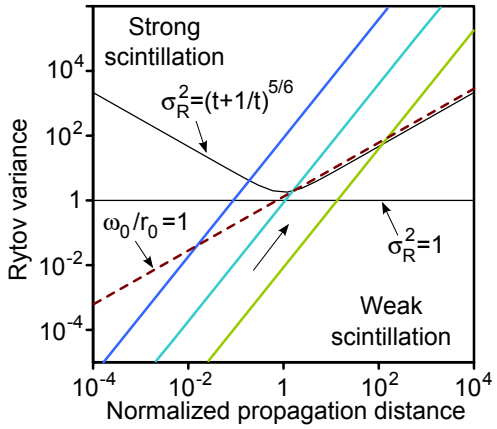

FIG. 7: A diagram showing the different regions of scintillation strength in terms of the Rytov variance σ_R^2 as a function of the normalized propagation distance t on a log-log scale. Weak scintillation lies toward the bottom and strong scintillation toward to top, with the boundaries between these two regions shown for both plane waves ($\sigma_R^2 = 1$) and Gaussian beams [$\sigma_R^2 = (t + 1/t)^{5/6}$]. The dashed line ($\omega_0/r_0 = 1$) is where the concurrence goes to zero according to the single phase screen calculations and the three slanted coloured lines indicate the increase in σ_R^2 with propagation distance for different strengths of turbulence — stronger turbulence toward the left and weaker turbulence toward the right.

If one uses Eq. (15) as the indication of strong scintillation, then it seems that, according to the single phase screen calculations, one never reaches the strong scintillation region with a nonzero concurrence, which implies that the single phase screen approximation can be used for all situations. There are however, a few caveats:

- Is it valid to use Eq. (15) as the indication of strong scintillation for the case of quantum entanglement decay?
- When the original qubit is prepared in terms of basis states with larger OAM the entanglement lasts longer, according to calculations in the single phase screen approximation [8]. As a result, larger values of OAM give entangled states that can retain their entanglement deeper into the region of strong scintillation.
- The calculations of the concurrence were made with the aid of the quadratic structure function approximation [8]. How accurate is this approximation in this situation?

These issues justify the use of a different more accurate approach. Next we follow an infinitesimal propagation approach, which is valid for all strengths of scintillation and does not require the quadratic structure function approximation.

IV. INFINITESIMAL PROPAGATION EQUATION

1. Operator product expansion [12]

Instead of doing the calculation in one step, going from the pure initial state to the final mixed state, one can break the process up into infinitesimally small steps. In each step the infinitesimal propagation process operates on the density operator of a (potentially) mixed state and produces a slightly perturbed version of this density operator

$$\rho(z) \to \rho(z + dz) = dU\rho(z)dU^\dagger. \tag{35}$$

Here dU represents the unitary operator for an infinitesimal propagation through turbulence. Again the ensemble averaging can be expression as a summation over the ensemble elements

$$\rho(z + dz) = \langle dU\rho(z)dU^\dagger \rangle = \sum_s^N \frac{1}{N} dU_s\rho(z)dU_s^\dagger, \tag{36}$$

where, as before, the subscript s denotes a particular instance of the refractive index fluctuations. In terms of the density matrix elements for a single photon this becomes

$$\rho_{mn}(z+dz) = \sum_{s}^{N} \frac{1}{N} \langle m|dU_s|p\rangle \rho_{pq}(z) \langle q|dU_s^{\dagger}|n\rangle, \tag{37}$$

with implied summations over p and q. We'll first consider the density matrix for a single photon and then generalize it to the bipartite case with two photons.

2. Field transformation

Although the single phase screen approximation is valid in this situation, thanks to the short propagation distances, the fact that this operation is performed repeatedly implies that one also needs to include the free space propagation process, which is neglected in the Paterson model.[a] As a result dU will contain a propagation term in addition to the random phase modulation term. To find the correct expression for dU we start with the equation of motion in turbulence, which is given by [1]

$$\nabla_T^2 g(\mathbf{x}) - i2k_0 \partial_z g(\mathbf{x}) + 2k_0^2 \delta n(\mathbf{x}) g(\mathbf{x}) = 0. \tag{38}$$

Here k_0 is the wave number, $g(\mathbf{x})$ represents the scalar electromagnetic field and $\delta n(\mathbf{x})$ is the fluctuations in the refractive index. The expression in Eq. (38) is obtained from the Helmholtz equation under the paraxial approximation, which assumes that the optical field propagates close to the beam axis (in this case the z-axis) and under the assumption that $\delta n \ll \langle n \rangle \approx 1$. The conditions for both these approximations are well satisfied in our situation.

In the two-dimensional transverse Fourier domain, Eq. (38) becomes

$$-|\mathbf{K}|^2 G(\mathbf{K}, z) - i2k_0 \partial_z G(\mathbf{K}, z) + 2k_0^2 N(\mathbf{K}, z) \star G(\mathbf{K}, z) = 0, \tag{39}$$

where $\mathbf{K} = k_x \hat{x} + k_y \hat{y}$ is the two-dimensional transverse Fourier domain coordinate vector, $G(\mathbf{K}, z)$ and $N(\mathbf{K}, z)$ are the two-dimensional transverse Fourier transforms of $g(\mathbf{x})$ and $\delta n(\mathbf{x})$, respectively, and $\star$ denotes convolution. It then follows that

$$G(\mathbf{K}, z_0 + dz) = G(\mathbf{K}, z_0) + \frac{idz}{2k_0} \left[|\mathbf{K}|^2 G(\mathbf{K}, z_0) - 2k_0^2 N(\mathbf{K}, z_0) \star G(\mathbf{K}, z_0) \right]. \tag{40}$$

One can use $G(\mathbf{K}, z)$ to define a quantum state in terms of a two-dimensional momentum basis. For instance,

$$|m\rangle = \int G_m(\mathbf{K}, z) |\mathbf{K}\rangle \, \frac{\mathrm{d}^2 k}{(2\pi)^2}, \tag{41}$$

where $|\mathbf{K}\rangle$ denotes the two-dimensional momentum basis elements and $G_m(\mathbf{K}, z) = \langle \mathbf{K}|m\rangle$. Note that if we substitute $G(\mathbf{K}, z_0) = G_m(\mathbf{K}, z_0)$ in Eq. (40), then one cannot assume that the transformed wave function is still associated with the same basis element $G(\mathbf{K}, z_0 + dz) \neq G_m(\mathbf{K}, z_0 + dz)$. This is due to the distortion introduced by the noise term that contains $N(\mathbf{K}, z_0)$.

3. Infinitesimal propagation equation

Here we do not show the complete derivation of the infinitesimal propagation equation (IPE). For a derivation of the IPE see [21].

The expression for the infinitesimal propagation equation (IPE) for a single photon propagating through turbulence, is given by

$$\partial_z \rho_{mn}(z) = i\mathcal{P}_{mp}(z)\rho_{pn}(z) - i\rho_{mp}(z)\mathcal{P}_{pn}(z) + \Lambda_{mnpq}(z)\rho_{pq}(z) - \Lambda_T \rho_{mn}(z), \tag{42}$$

---

[a] One can neglect the propagation process in Paterson's model, because the inner products before and after a single propagation will give the same result.

where the first two terms represent a commutator between the density matrix and the 'free Hamiltonian,' (the kinetic term)[b] given by

$$\mathcal{P}_{mp}(z) = \frac{1}{2k_0}\int |\mathbf{K}|^2 G_m^*(\mathbf{K},z)G_p(\mathbf{K},z)\ \frac{\mathrm{d}^2k}{(2\pi)^2}, \tag{43}$$

and the last two terms represent the dissipative (or interaction) terms, where

$$\Lambda_{mnpq} = k_0^2\int W_{mp}^*(\mathbf{K},z)W_{nq}(\mathbf{K},z)\Phi_0(\mathbf{K},0)\ \frac{\mathrm{d}^2k}{(2\pi)^2}, \tag{44}$$

with

$$W_{mn}(\mathbf{K},z) = \int G_m(\mathbf{K}'+\mathbf{K},z)G_n^*(\mathbf{K}',z)\ \frac{\mathrm{d}^2k'}{(2\pi)^2}, \tag{45}$$

and

$$\Lambda_T = k_0^2\int \Phi_0(\mathbf{K},0)\ \frac{\mathrm{d}^2k}{(2\pi)^2}. \tag{46}$$

4. Index symmetries

Based on their definitions and the fact that the power spectral density is symmetric [$\Phi_0(\mathbf{K},0) = \Phi_0(-\mathbf{K},0)$], W_{mn} and Λ_{mnpq} obey the following properties,

$$W_{mn}(\mathbf{K},z) = W_{nm}^*(-\mathbf{K},z), \tag{47}$$

and

$$\Lambda_{mnpq} = \Lambda_{qpnm} = \Lambda_{nmqp}^*. \tag{48}$$

5. Generalizations

We now generalize the single photon expression in Eq. (42) for two-photon (bipartite) states. The density operator for a bipartite state becomes a tensor contracted with the bra- and ket-basis vectors for both photons

$$\rho = \sum_{m,n} |m\rangle_A|p\rangle_B \rho_{mnpq}\langle n|_A\langle q|_B. \tag{49}$$

where $|m\rangle$ and $\langle n|$ are the ket- and bra-basis vectors, respectively, for the one photon (A-subsystem) and $|p\rangle$ and $\langle q|$ are the ket- and bra-basis vectors for the other photon (B-subsystem).

First we consider the case where only one of the two photons propagates through turbulence. The other photon is assumed to propagate through free-space without turbulence. The IPE for this case contains the free-space kinetic terms for both photons, but only dissipative terms for one of the photons. The resulting expression is given by

$$\partial_z\rho_{mnpq} = i\left(\mathcal{P}_{mx}\rho_{xnpq} - \rho_{mxpq}\mathcal{P}_{xn} + \mathcal{P}_{px}\rho_{mnxq} - \rho_{mnpx}\mathcal{P}_{xq}\right) + \Lambda_{mnxy}\rho_{xypq} - \Lambda_T\rho_{mnpq}. \tag{50}$$

In the case where both photons propagate through turbulence, but along different paths so that the turbulent media are uncorrelated, the expression contains dissipative terms for both photons [21]

$$\partial_z\rho_{mnpq} = i\left(\mathcal{P}_{mx}\rho_{xnpq} - \rho_{mxpq}\mathcal{P}_{xn} + \mathcal{P}_{px}\rho_{mnxq} - \rho_{mnpx}\mathcal{P}_{xq}\right) + \Lambda_{mnxy}\rho_{xypq} + \Lambda_{pqxy}\rho_{mnxy} - 2\Lambda_T\rho_{mnpq}. \tag{51}$$

If the two photons propagate through the same turbulence, the expression contains additional dissipative terms due to the correlations between the two photons [22]

$$\begin{aligned}\partial_z\rho_{mnpq} \;=\; & i\left(\mathcal{P}_{mx}\rho_{xnpq} - \rho_{mxpq}\mathcal{P}_{xn} + \mathcal{P}_{px}\rho_{mnxq} - \rho_{mnpx}\mathcal{P}_{xq}\right) + \Lambda_{mnxy}\rho_{xypq} + \Lambda_{pqxy}\rho_{mnxy} \\ & + \Lambda_{mqxy}\rho_{xnpy} + \Lambda_{pnxy}\rho_{myxq} - \Lambda_{xnqy}\rho_{mypx} - \Lambda_{mxyp}\rho_{ynxq} - 2\Lambda_T\rho_{mnpq}.\end{aligned} \tag{52}$$

[b] The terminology of 'Hamiltonian' and 'kinetic term' is used in analogy to the situation where the system evolves in time. Here the system evolves in z, along the propagation distance. Therefore, it is actually the z-component of the momentum operator (or the zz-component of the stress-energy tensor).

6. Solving the IPE

In its general form the IPE represents an infinite set of coupled first order differential equations — one for each element in the density matrix. In practice one needs to truncate the set of differential equations by truncating the modal basis that determines the size of the density matrix. This still leaves a large number of coupled first order differential equations. The smallest case of an entangled bipartite state (two entangled qubits) has a density matrix with 16 elements. For two qutrits the size grows to 81 elements. These are the only cases that have so far been considered. The bipartite qubit has been solved in [21] and the bipartite qutrit has been solved in [23].

To solve the IPE, one first needs to evaluate the integrals for $\mathcal{P}_{mn}$ and Λ_{mnpq} and Λ_T, which are given in Eqs. (43), (44) and (46), respectively, for a given basis. Here we'll use the LG basis. Once these integrals have been evaluated, one can form the set of coupled differential equations that needs to be solved.

7. Generating function for the LG modes

In terms of normalized coordinates the Laguerre-Gaussian (LG) modes can be expressed as

$$U_{p,\ell}^{LG}(u,v,t) = \left[\frac{2\pi p! 2^{|l|}}{(p+|l|)!}\right]^{1/2} \frac{(u \pm iv)^{|\ell|}(1+it)^p}{(1-it)^{p+|\ell|+1}} L_p^{|\ell|}\left[\frac{2(u^2+v^2)}{1+t^2}\right] \exp\left(\frac{u^2+v^2}{it-1}\right), \tag{53}$$

where $L_p^{|\ell|}$ represents the associate Laguerre polynomials [24]; the normalized coordinates are defined as $u = x/w_0$, $v = y/w_0$ and $t = z/z_R = z\lambda/\pi w_0^2$, in terms of the initial radius of the mode profile w_0 and the Rayleigh range z_R; p is the radial index (a non-negative integer); ℓ is the azimuthal index (a signed integer); and the $\pm$ sign is given by the sign of ℓ. The LG modes represents an OAM basis, because the OAM of the photons in an LG mode is quantized with a value proportional to the azimuthal index ℓ.

The integrals in Eqs. (43), (44) and (46), all involve the expressions of the LG modes in the Fourier domain. To alleviate the evaluation of these integrals we use the generating function for the angular spectra of the LG modes. The generating function for the LG modes, in terms of the normalized coordinates of Eq. (53), is given by

$$G = \frac{i}{\Omega(t,\eta)} \exp\left[i\frac{(u+iv)\xi + (u-iv)\zeta - (1+\eta)(u^2+v^2)}{\Omega(t,\eta)}\right], \tag{54}$$

where $\Omega(t,\eta) = (1+\eta)t + i(1-\eta)$. The parameters ξ, ζ and η are used to generate particular LG modes in the following way,

$$U_{p,\ell}^{LG}(u,v,t) = \begin{cases} \mathcal{N}\left[\frac{1}{p!}\partial_\eta^p \partial_\xi^{|\ell|} G\right]_{\eta,\xi,\zeta=0} & \text{for} \quad \ell > 0 \\ \mathcal{N}\left[\frac{1}{p!}\partial_\eta^p G\right]_{\eta,\xi,\zeta=0} & \text{for} \quad \ell = 0 \\ \mathcal{N}\left[\frac{1}{p!}\partial_\eta^p \partial_\zeta^{|\ell|} G\right]_{\eta,\xi,\zeta=0} & \text{for} \quad \ell < 0, \end{cases} \tag{55}$$

where

$$\mathcal{N} = \left[\frac{p! 2^{|\ell|+1}}{\pi(p+|\ell|)!}\right]^{1/2}. \tag{56}$$

The Fourier transform of the generating function is given by

$$\mathcal{F}\{G\} = \frac{\pi}{1+\eta} \exp\left[i\frac{\pi(a+ib)\xi + \pi(a-ib)\zeta + \pi^2(a^2+b^2)\Omega(t,\eta)}{1+\eta}\right], \tag{57}$$

where a and b are normalized spatial frequency components that are related to k_x and k_y through

$$k_x = \frac{2\pi a}{w_0} \qquad k_y = \frac{2\pi b}{w_0}. \tag{58}$$

The angular spectra of the LG modes are obtained from Eq. (57), by using the same procedure given in Eq. (55).

8. Von Karman power spectral density

The IPE allows one to use any power spectral density $\Phi_0(\mathbf{k})$ for the turbulence. Here we'll neglect the effect of the inner scales, and use the von Karman power spectral density [1],[c]

$$\Phi_0(\mathbf{k}) = \frac{0.033(2\pi)^3 C_n^2}{(|\mathbf{k}|^2 + \kappa_0^2)^{11/6}} = \Phi_1(K), \tag{59}$$

where κ_0 is inversely proportional to the outer scale of the turbulence. The outer scale helps to regularize the integrals, but in the limit of large outer scale ($\kappa_0 \to 0$) it disappears from the final expressions. Since the power spectral density only depends on the magnitude of $\mathbf{k}$, one can set $k_z = 0$ (see [21]), so that $\mathbf{k}$ is replaced by $K = |\mathbf{K}|$.

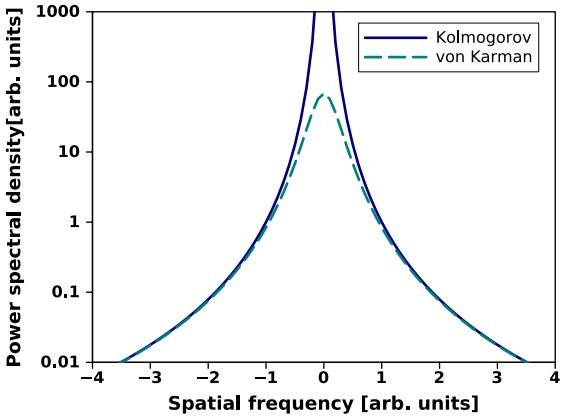

FIG. 8: Comparison of von Karman and Kolmogorov power spectral densities.

Figure 8 shows the difference between the von Karman and the Kolmogorov power spectral densities.

9. Free-space propagation operator

First we consider the integral in Eq. (43), which represents the free-space propagation. After evaluating the integral and removing the superfluous mixed terms containing the ξ's and ζ's of the same photon, we obtain a generating function for the $\mathcal{P}_{mn}$-integral,

$$\mathcal{P}_G = \frac{\pi(1+\eta_m)(1+\eta_n)}{8(1-\eta_m\eta_n)^3 z_R} \exp\left[\frac{\xi_m\xi_n + \zeta_m\zeta_n}{2(1-\eta_m\eta_n)}\right] \left[2(1-\eta_m\eta_n) + \xi_m\xi_n + \zeta_m\zeta_n\right], \tag{60}$$

where ξ_m, ξ_n, ζ_m, ζ_n, η_m, and η_n are the generating function parameters, associated with the m- and n-indices. Since the ξ's (or ζ's) always appear in products for the m- and n-indices, the result implies an orthogonality condition for the azimuthal indices. The same is not true for the radial indices — one finds that the result is non-zero when the radial indices differ by either 0 or 1. All other cases gives zero. When the difference between the radial indices is 0 the final result for explicit modes can be expressed as

$$\mathcal{P}_{mn} = \frac{1 + |\ell| + 2p}{2z_R}, \tag{61}$$

where the azimuthal indices are indicated by $\ell_m = \ell_n = \ell$ and the radial indices are indicated by $p_m = p_n = p$. When the difference between the radial indices is equal to 1 the result for explicit modes is given by

$$\mathcal{P}_{mn} = \frac{(1 + |\ell| + p)^{1/2}(1+p)^{1/2}}{2z_R} \tag{62}$$

where the azimuthal indices are again indicated by $\ell_m = \ell_n = \ell$, but now the radial indices are indicated by $p = (p_m + p_n - 1)/2$.

[c] The definition here differs from that found in [1], by a factor of $(2\pi)^3$, which is the result of a difference in the way we use the 2π-factors in our Fourier integrals.

10. Divergent dissipative term

Next we consider the integral for the dissipative term given in Eq. (46). Substituting Eq. (59) into Eq. (46), one obtains

$$\Lambda_T = \frac{(2\pi)^2\Gamma(2/3)}{\sqrt{3}}\frac{C_n^2}{\lambda^2\kappa_0^{5/3}} = \frac{30.86\ C_n^2}{\lambda^2\kappa_0^{5/3}}. \tag{63}$$

Hence, Λ_T diverges for large outer scale ($\kappa_0 \to 0$). However, we'll find that these terms are canceled by similar terms coming from $\Lambda_{mnuv}(z)$.

11. Modal correlation functions

The integral in Eq. (45) represents the correlation between the angular spectra of the OAM modes. To evaluate this integral we express the generating function of Eq. (57) in normalized cylindrical momentum space coordinates, so that $k_x + ik_y = K\exp(i\phi)/w_0$. The result of the integration, left as a generating function, is given by

$$\begin{aligned} W_G &= \frac{\pi}{2(1-\eta_m\eta_n)}\exp\left[\frac{\xi_m\xi_n+\zeta_m\zeta_n}{2(1-\eta_m\eta_n)} - \frac{K^2\Omega_m\Omega_n^*}{8(1-\eta_m\eta_n)}\right. \\ &\quad \left. + \frac{K\exp(i\phi)(\zeta_n\Omega_m - \xi_m\Omega_n^*)}{4(1-\eta_m\eta_n)} + \frac{K\exp(-i\phi)(\xi_n\Omega_m - \zeta_m\Omega_n^*)}{4(1-\eta_m\eta_n)}\right], \end{aligned} \tag{64}$$

where $\Omega_m = \Omega(t,\eta_m)$ and $\Omega_n^* = \Omega^*(t,\eta_n)$. If we evaluate the azimuthal indices explicitly while leaving the radial indices implicit in terms of the parameter η_m and η_n, and multiply it with the the normalization constants in Eq. (56), one can express the correlation function as

$$\begin{aligned} W_{rG} &= \left[\frac{p_n!}{(|n|+p_n)!}\right]^{1/2}\left[\frac{p_m!}{(|m|+p_m)!}\right]^{1/2}\frac{\exp(-X)\exp[i(m-n)\phi](\kappa_m)^{|n|}(-\kappa_n^*)^{|m|}}{(1-\eta_m\eta_n)} \\ &\quad \times \sum_{s=0}^{M(m,n)}\frac{|m|!|n|!}{(-X)^s(|m|-s)!(|n|-s)!s!}, \end{aligned} \tag{65}$$

where $m(=\ell_m)$ and $n(=\ell_n)$ are the azimuthal indices; p_m and p_n are their associated radial indices; and

$$M(m,n) = \frac{1}{2}\left(|m|+|n|-|m-n|\right) \tag{66}$$

$$\kappa_m = \frac{K\Omega_m}{2\sqrt{2}(1-\eta_m\eta_n)} \tag{67}$$

$$\kappa_n^* = \frac{K\Omega_n^*}{2\sqrt{2}(1-\eta_m\eta_n)} \tag{68}$$

$$X = \frac{K^2\Omega_m\Omega_n^*}{8(1-\eta_m\eta_n)} = \kappa_m\kappa_n^*(1-\eta_m\eta_n). \tag{69}$$

Note that W_{rG} still represents a generating function with respect to the radial indices, even though the radial indices also appear explicitly due to the normalization constant.

12. Special case: zero radial index, $p = 0$

A special case that is often encountered, is when the radial index of the LG modes are set to zero. This implies that the generating parameters for the radial index are set equal to zero ($\eta_m = \eta_n = 0$) in Eqs. (65) to (69) . The result then simplifies to

$$\begin{aligned} W_{mn} &= (-1)^{|m|}Y^{(|n|+|m|)/2}\exp(-Y)\exp[i(m-n)\phi]\exp[i(|n|-|m|)\gamma] \\ &\quad \times \sum_{s=0}^{M(m,n)}\frac{\sqrt{|m|!}\sqrt{|n|!}}{(-Y)^s(|m|-s)!(|n|-s)!s!}, \end{aligned} \tag{70}$$

where

$$Y = \frac{K^2}{8}(1+t^2) \tag{71}$$

$$\exp(i\gamma) = \sqrt{\frac{t+i}{t-i}}. \tag{72}$$

Note that γ is the Gouy phase.

13. General dissipative term

The two-dimensional integration in Eq. (44) can be separated into a radial and angular integral in cylindrical momentum space coordinates. Since $\Phi_1(K)$ only depends on the radial coordinate ($K = |\mathbf{K}|$) the integral over ϕ only involves the ϕ-dependencies of the W's, as expressed in Eq. (65), or Eq. (70) for $p = 0$. The combined ϕ-dependencies of the two W's is given by $\exp[i(m-u-n+v)\phi]$, where m, n, u and v are the azimuthal indices of all the modes involved. The result of the angular integral is zero unless $m-u-n+v=0$, in which case the result is 2π times the product of the two W's without the ϕ-dependent exponentials. As a result, many of the elements in Λ_{mnuv} vanish.

The result of the remaining K-integral is too complicated to express as a single closed form expression. However, one can consider the result on a term-by-term basis. These terms all have the form

$$f_j(K) = \frac{A\exp(-BK^2)K^{2j}}{(K^2+\kappa_0^2)^{11/6}}, \tag{73}$$

where j is a non-negative integer, A contains all the multiplicative parameters from Eqs. (65) and (59), and B is a parameter composed of the parameters in the exponent of Eq. (65), as given in Eq. (69).

If $j = 0$ the integral over $f_j(K)$ diverges as $\kappa_0 \to 0$. In the limit of small κ_0 the leading terms are,

$$\int_{-\infty}^{\infty} f_0(K)K\ \mathrm{d}K = \Lambda_T - \frac{\pi^{1/2}(2\pi)^3}{6\Gamma(2/3)}\frac{C_n^2 w_0^{5/3}(1+t^2)^{5/6}}{\lambda^2} = \Lambda_T - \frac{\sigma}{z_R}(1+t^2)^{5/6}, \tag{74}$$

where Λ_T is given by Eq. (63) and

$$\sigma = \frac{\pi^{3/2}C_n^2 w_0^{11/3}}{6\Gamma(2/3)\lambda^3}. \tag{75}$$

It turns out that the Λ_T-term in Eq. (51) exactly cancels off all the Λ_T-terms that appear inside the Λ_{mnpq}-term in Eq. (51) as a result of Eq. (74).

The integrals of $f_j(K)$ with $j > 0$ all give finite results independent of κ_0 in the limit where $\kappa_0 \to 0$, and have the form,

$$\int_{-\infty}^{\infty} f_j(K)K\ \mathrm{d}K = \frac{G_j\sigma}{z_R}(1+t^2)^{5/6}, \tag{76}$$

where G_j is a numerical constant that only depends on j,

$$G_j = (-1)^{j+1}\frac{5}{12}\frac{2^{1/3}3^{1/2}\Gamma(2/3)^2}{2^m\pi^{1/2}\Gamma(11/6-j)}. \tag{77}$$

14. Example: symmetric bipartite qubit

Here we work through a simple example [21] where only modes of the lowest radial index ($p = 0$) and with azimuthal indices $\ell = \pm 1$ are considered. The small number of modes (only two in this case) imply a severe truncation. The trace of the truncated density matrix is not in general equal to 1. The truncated density matrix can be normalized to calculate the concurrence [5, 6] as a measure of the entanglement. On the other hand, the reduced trace gives an indication of the loss of information to the higher order modes.

For $p = 0$ one sets $w_1 = w_2 = 0$ in all the generating functions. Then all the non-dissipative terms (those that contain $\mathcal{P}$) in Eq. (51) are equal and cancel each other, so that only the dissipative terms remain.

After evaluating the integrals for $\Lambda_{m,n,u,v}(z)$ one finds that, in the limit of large outer scale, the only nonzero elements are

$$\Lambda_{1,1,1,1} = \Lambda_{-1,1,-1,1} = \Lambda_{1,-1,1,-1} = \Lambda_{-1,-1,-1,-1} = \Lambda_T - \frac{259}{144}\frac{\sigma}{z_R}(1+t^2)^{5/6} \tag{78}$$

and

$$\Lambda_{1,1,-1,-1} = \Lambda_{-1,-1,1,1} = \frac{5}{144}\frac{\sigma}{z_R}(1+t^2)^{5/6}. \tag{79}$$

The elements in Eq. (78), which contain the diverging Λ_T from Eq. (63), are the diagonal elements of $\Lambda_{mnuv}(z)$ when treated as a 4×4 matrix. One can therefore view Λ_T in Eq. (78) as being multiplied by an identity matrix. The Λ_T-term in Eq. (51) also represents an identity matrix, but with the opposite sign. This implies that the Λ_T-term in Eq. (51) exactly cancels the Λ_T-elements in Eq. (78) for both $\Lambda_{mnuv}(z)$-terms in Eq. (51), leaving the final expression without Λ_T. As a result, one can take the limit $\kappa_0 \to 0$ to obtain a final expression that is finite and independent of κ_0.

Assuming that the initial state of the density matrix is the singlet Bell-state in the OAM basis $(|q\rangle|\overline{q}\rangle - |\overline{q}\rangle|q\rangle)/\sqrt{2}$, one obtains the following solution for the truncated density matrix,

$$\rho_{mnpq} = \frac{T}{4}\begin{bmatrix} 1-R^2 & 0 & 0 & 0 \\ 0 & 1+R^2 & -2R & 0 \\ 0 & -2R & 1+R^2 & 0 \\ 0 & 0 & 0 & 1-R^2 \end{bmatrix}, \tag{80}$$

where mp (nq) denote the row (column) indices, and

$$T = \exp\left[-\frac{127}{36}Z(t)\right] \qquad R = \exp\left[-\frac{5}{72}Z(t)\right], \tag{81}$$

with

$$Z(t) \equiv \sigma \int_0^t (1+\tau^2)^{5/6}\, \mathrm{d}\tau. \tag{82}$$

The eigenvalues of the truncated density matrix in Eq. (80) are $T(1+R)^2/4$, $T(1-R)^2/4$, $T(1-R^2)/4$ and $T(1-R^2)/4$, which are all positive. The trace of the truncated density matrix is given by T in Eq. (81), which is a decaying function. The trace indicates how much of the information is lost due to coupling to higher order modes that are not represented in the density matrix. Normalizing the density matrix by setting $T = 1$, one can calculate the concurrence [5, 6], as given in Eq. (18), to obtain

$$\mathcal{C} = \frac{1}{2}(R^2 + 2R - 1). \tag{83}$$

The shape of the concurrence curve as a function of the scintillation strength is shown in Fig. 9 for three cases where $\ell = \pm1, \pm2, \pm3$, respectively.

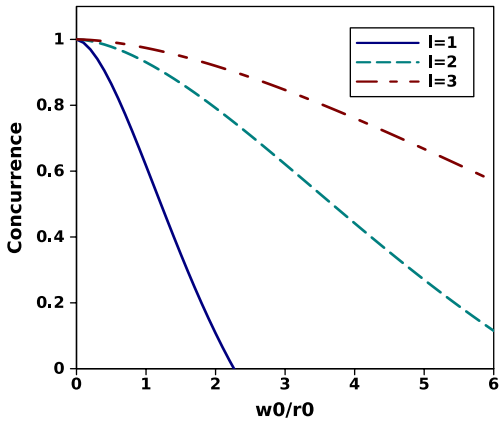

FIG. 9: Concurrence of initial Bell singlets with $\ell = \pm1, \pm2, \pm3$, respectively, as a function of scintillation strength, according to the IPE.

Comparing the curves in Fig. 9 to those in Fig. 6, we see that for larger values of ℓ the IPE seems to underestimate the rate of entanglement decay. This is the result of truncation, which excludes the elements between $|\ell\rangle$ and $|-\ell\rangle$. Although the IPE can keep track of the loss of amplitude to the excluded elements, it cannot observe the amplitude that couples back from such excluded elements. As a result it underestimates the coupling between elements that are far apart. Truncation affects the single phase screen calculations [8] less, because the single phase screen approach incorporates multiple scattering, which compensates for the coupling to and from the excluded elements.

15. Strong turbulence — fast decay of entanglement

One can evaluate the integral in Eq. (82) to obtain

$$\int_0^t (1+\tau^2)^{5/6}\,\mathrm{d}\tau = t\ {}_2\mathrm{F}_1\left(\left[-\frac{5}{6},\frac{1}{2}\right],\left[\frac{5}{2}\right],-t^2\right) = t + \mathrm{O}(t^3) \tag{84}$$

where ${}_2\mathrm{F}_1([\cdot],[\cdot],\cdot)$ is the Barnes extended hypergeometric functions [25].

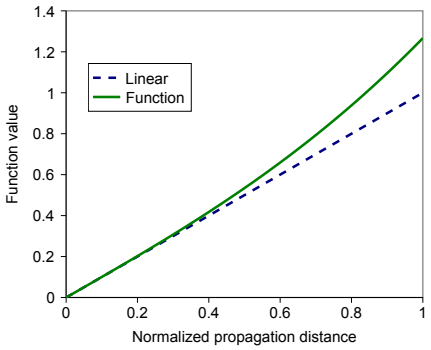

FIG. 10: Comparison of von Karman and Kolmogorov power spectral densities.

For small t (where $t \lesssim 1/3$) the result of the integral in Eq. (84) is approximately equal to t. In Fig. 10 the shape of the function in Eq. (84) is compared with t. For propagation distances much shorter than the Rayleigh range the integral in Eq. (82) can be approximated by,

$$Z(t) \approx \sigma t \approx \frac{13}{4}\left(\frac{w_0}{r_0}\right)^{5/3}, \tag{85}$$

where r_0 is the Fried parameter, given in Eq. (31). Thus all the dimension parameters are combined into w_0/r_0. If the entanglement completely decays over distances much shorter than the Rayleigh range (i.e. in the fast decay limit) one can use Eq. (85) and thus express the entire behaviour simply as a function of w_0/r_0, as was found in the single phase screen calculations [8]. For larger values of t the behaviour becomes more complicated, as shown by the function in Eq. (84). In that case the behaviour does not only depend on w_0/r_0 but also on

$$\left[\frac{w_0}{r_0}\right]_{z=z_R} = \frac{10.74(C_n^2)^{3/5}w_0^{11/5}}{\lambda^{9/5}}. \tag{86}$$

V. ROBUST STATES

1. Definition of a robust state

Here we investigate whether a quantum state can be optimized so that it will retain as much of its initial entanglement as possible, while propagating in a turbulent atmosphere [23]. Such an optimized quantum state is called a robust state. We consider bipartite qutrit states in the LG basis, consisting of the three elements with $p = 0$ and $\ell = 1, 0, -1$. The two photons are assumed to propagate through different uncorrelated regions of atmospheric turbulence. We use the IPE to calculate the density matrix as a function of the propagation distance. The turbulence is modeled by the Kolmogorov power spectral density Eq. (13), or Eq. (73) with $\kappa_0 \to 0$.

2. Tangle

The concurrence [5, 6] is a suitable measure of entanglement for two-dimensional bipartite systems, but for higher-dimensional states it is demanding to compute it directly. Instead, we use the tangle $\tau\{\rho\}$,

$$\tau\{\rho\} = 2\ \mathrm{tr}\{\rho^2\} - \mathrm{tr}\{\rho_\mathrm{A}^2\} - \mathrm{tr}\{\rho_\mathrm{B}^2\}, \tag{87}$$

where ρ_{A} and ρ_{B} are the respective reduced density matrices of the two subsystems. The tangle is equal to the square of the concurrence for pure states and gives a lower bound for that of mixed quantum states [26]. For a maximally entangled state $\tau = \tau_{\max} = 2(d-1)/d$, where d is the dimension of the subsystems' Hilbert spaces, and for a separable state $\tau = \tau_{\min} = 0$.

To find the robust qutrit states, we optimize the tangle at a given propagation distance $z > 0$. The result is expressed in terms of the parameters for the initial pure state that will give the maximum tangle at that propagation distance.

3. Propagation distance functions

After solving the differential equations of the IPE to obtain the density matrix as a function of the propagation distance, one finds that its dependence on the propagation distance is governed by $Z(t)$, as given in Eq. (84), and by the integral

$$H(t) \equiv \int_0^t (1+\tau^2)^{5/6} \left(\frac{1+\mathrm{i}\tau}{1-\mathrm{i}\tau}\right) \,\mathrm{d}\tau, \tag{88}$$

where t is the normalized propagation distance Eq. (16). For convenience we separate $H(t)$ into its real and imaginary parts $H(t) \equiv H_{\mathrm{r}}(t) + \mathrm{i}H_{\mathrm{i}}(t)$. These integrals can be solved to give expressions in terms of hypergeometric functions

$$H_{\mathrm{r}}(t) = \frac{11}{8}\,{}_2\mathrm{F}_1\left(\left[\frac{1}{6},\frac{1}{2}\right],\left[\frac{1}{2}\right],-t^2\right) t - \frac{2}{8}\left(1+t^2\right)^{5/6} \tag{89}$$

$$H_{\mathrm{i}}(t) = \frac{6}{5}\left[(1+t^2)^{5/6}-1\right], \tag{90}$$

where ${}_2\mathrm{F}_1([\cdot],[\cdot],\cdot)$ represents the Barnes extended hypergeometric functions [25].

4. Factorization law

If one party of a bipartite (or multipartite) state propagates through a dissipative channel (such as a turbulent atmosphere), the final state's entanglement is proportional to the initial state's entanglement [27–30]. Hence, the shape of the decay curve is independent of the initial entanglement. In such a case the initially state can not be optimized — the maximally entangled states are the robust states.

This is also true where all parties of an entangled state pass through trace preserving dissipative channels [31]. However, if both parties of an entangled bipartite state pass through uncorrelated dissipative channels that are not trace preserving, only an upper bound exists for the evolution of the entanglement [27–29]. In such a case the initially states can not be optimized to give robust states that are different from the maximally entangled states. Here we consider the case where the channel is not trace preserving due to post selection, which truncates the state to a finite Hilbert space.

5. Initial state

We'll obtain the robust states by optimizing the tangle for the most general pure bipartite qutrit state that can be defined in terms of the Hilbert space $\mathcal{H}_3 \otimes \mathcal{H}_3$. In its most general form a pure bipartite qutrit state is expressed by

$$|\psi\rangle = \sum_{m,n} c_{m,n}|m\rangle|n\rangle, \tag{91}$$

where $c_{m,n}$ represents complex coefficients and $|m\rangle$ and $|n\rangle$ are OAM eigenstates (LG modes) in the respective subsystems, with azimuthal indices $m, n \in \{1, 0, -1\}$. The normalization of the initial state implies that

$$\sum_{m,n} |c_{m,n}|^2 = 1. \tag{92}$$

The nine complex coefficients in Eq. (91) represent 18 real degrees of freedom. The normalization condition of Eq. (92) removes one of these real degrees of freedom and the overall phase factor that can be ignored implies the removal of another real degree of freedom. As a result one needs 16 real degrees of freedom to specify an arbitrary initial quantum state. These are divided into 8 parameters for the magnitudes of the coefficients and 8 parameters for the complex phase factors of the coefficients. Due to the form of the normalization condition

in Eq. (92), it is natural to represent the 8 parameters for the magnitudes of the coefficients in terms of sine and cosine functions. Therefore, the parameterization for the complex coefficients $c_{m,n}$ in Eq. (91) is given by

$$\begin{aligned}
c_{1,1} &= \sin(k_{\rm a})\sin(k_{\rm b})\sin(k_{\rm d})\sin(k_{\rm h})\exp[{\rm i}(q_{\rm a}+q_{\rm b}+q_{\rm d}+q_{\rm d})]\\
c_{1,-1} &= \cos(k_{\rm a})\sin(k_{\rm b})\sin(k_{\rm d})\sin(k_{\rm h})\exp[{\rm i}(-q_{\rm a}+q_{\rm b}+q_{\rm d}+q_{\rm h})]\\
c_{-1,1} &= \sin(k_{\rm c})\cos(k_{\rm b})\sin(k_{\rm d})\sin(k_{\rm h})\exp[{\rm i}(q_{\rm c}-q_{\rm b}+q_{\rm d}+q_{\rm h})]\\
c_{-1,-1} &= \cos(k_{\rm c})\cos(k_{\rm b})\sin(k_{\rm d})\sin(k_{\rm h})\exp[{\rm i}(-q_{\rm c}-q_{\rm b}+q_{\rm d}+q_{\rm h})]\\
c_{0,0} &= \cos(k_{\rm h})\exp(-{\rm i}q_{\rm h})\\
c_{1,0} &= \sin(k_{\rm e})\sin(k_{\rm f})\cos(k_{\rm d})\sin(k_{\rm h})\exp[{\rm i}(q_{\rm e}+q_{\rm f}-q_{\rm d}+q_{\rm h})]\\
c_{-1,0} &= \cos(k_{\rm e})\sin(k_{\rm f})\cos(k_{\rm d})\sin(k_{\rm h})\exp[{\rm i}(-q_{\rm e}+q_{\rm f}-q_{\rm d}+q_{\rm h})]\\
c_{0,1} &= \sin(k_{\rm g})\cos(k_{\rm f})\cos(k_{\rm d})\sin(k_{\rm h})\exp[{\rm i}(q_{\rm g}-q_{\rm f}-q_{\rm d}+q_{\rm h})]\\
c_{0,-1} &= \cos(k_{\rm g})\cos(k_{\rm f})\cos(k_{\rm d})\sin(k_{\rm h})\exp[{\rm i}(-q_{\rm g}-q_{\rm f}-q_{\rm d}+q_{\rm h})].
\end{aligned} \tag{93}$$

These parameters were chosen to follow the pattern imposed by the symmetries found in the couplings, discussed below.

6. Modal scattering

The probability amplitude (coupling strength) for a particular OAM basis element to be generated when another OAM basis element is scattered through the scintillation process, is stronger for adjacent OAM modes (those with the smallest difference in OAM) than between OAM modes that are further apart [7, 19].

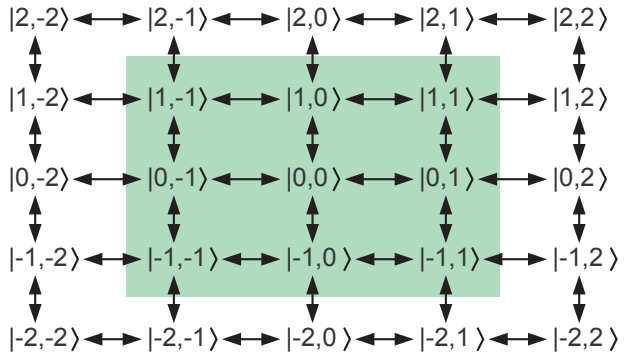

FIG. 11: Illustration of nearest neighbour couplings between the basis elements inside the $\mathcal{H}_3 \otimes \mathcal{H}_3$ Hilbert space (green background) and the coupling to basis elements outside (white background). Vertical arrows represent nearest neighbour couplings for the A-subsystem and horizontal arrows represent nearest neighbour couplings for the B-subsystem.

Figure 11 represents the nearest neighbour couplings between the OAM basis elements of the Hilbert space. The shaded (green) area represents the truncated $\mathcal{H}_3 \otimes \mathcal{H}_3$ Hilbert space that are included in the quantum state tomography measurements. The diagram also shows the neigbouring basis elements outside the Hilbert space. The dominant (nearest neighbour) couplings are represented by bidirectional arrows. The vertical arrows represent the couplings in the A-subsystem and the horizontal arrows represent the couplings in the B-subsystem.

7. Trace — Loss of photons

There is a loss of photons that is observed due to the post selection, introduced by the projective measurements in the truncated Hilbert space. This is directly given by the reduction in the trace of the unnormalized truncated density matrix.

The decay of the trace as a function of the propagation distance depends on the initial state, due to differences in the way the basis elements are scattered out of the truncated subspace. The basis elements are divided into three groups:

- $|0,0\rangle$: neighbouring states lie within the truncated Hilbert space.
- $\{|0,1\rangle, |1,0\rangle, |0,-1\rangle, |-1,0\rangle\}$: have one neighbouring state outside the truncated Hilbert space and three neighbouring states inside the truncated Hilbert space.

- $\{|1,1\rangle, |1,-1\rangle, |-1,1\rangle, |-1,-1\rangle\}$: have two neighbouring states outside the truncated Hilbert space and two neighbouring states inside the truncated Hilbert space.

These groups have progressively more neigbouring elements beyond the truncated Hilbert space.

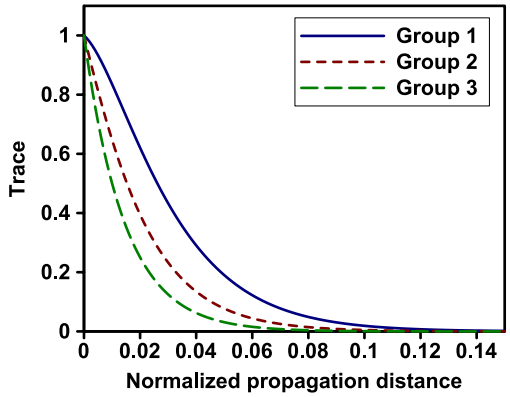

FIG. 12: Trace evolution of the truncated density matrix for strong turbulence. The graph contains three curves: solid (blue) line for the initial state from Group 1, short dashed (red) line for the initial state from Group 2 and long dashed (green) line for the initial state from Group 3.

Figure 12 shows the trace for initial states composed of elements from the three respective groups, while propagating through strong turbulence ($\sigma = 25$). The difference in coupling to states beyond the truncated Hilbert space manifests as a difference in the slope of the curve as it moves away from $t = 0$. Note that the state $|0,0\rangle$, which has the best performance of the three cases is not an entangled state.

8. Bell states

two-dimensional, composed from OAM states with the azimuthal indices $\ell = \pm 1$, one can show that the entanglement of the four maximally entangled Bell states, quantified by the concurrence, all decay equally [21]. This can be understood as a result of the fact that the scattering is symmetric with respect to $\ell = 1$ and $\ell = -1$. For a three-dimensional Hilbert space with $\ell = 1, 0, -1$, one can form 12 Bell states in the two-dimensional subspaces of our three-dimensional Hilbert space. These Bell states form three sets based on their decay curves

$$\text{Set 1} = \left\{\left|\Phi^+_{0,1}\right\rangle, \left|\Phi^+_{0,-1}\right\rangle, \left|\Phi^-_{0,1}\right\rangle, \left|\Phi^-_{0,-1}\right\rangle\right\} \tag{94}$$

$$\text{Set 2} = \left\{\left|\Psi^+_{0,1}\right\rangle, \left|\Psi^+_{0,-1}\right\rangle, \left|\Psi^-_{0,1}\right\rangle, \left|\Psi^-_{0,-1}\right\rangle\right\} \tag{95}$$

$$\text{Set 3} = \left\{\left|\Phi^+_{1,-1}\right\rangle, \left|\Phi^-_{1,-1}\right\rangle, \left|\Psi^+_{1,-1}\right\rangle, \left|\Psi^-_{1,-1}\right\rangle\right\}, \tag{96}$$

where $\left|\Phi^\pm_{r,s}\right\rangle$ and $\left|\Psi^\pm_{r,s}\right\rangle$ are the Bell states of the two-dimensional subspaces spanned by r and s, defined in Eq. (22) for $r = 0$ and $s = 1$. The decay curves are shown in Fig. 13.

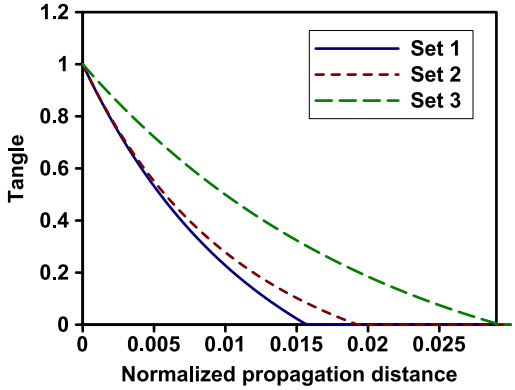

FIG. 13: Comparison of the tangle evolution of the Bell states in Set 1, Set 2 and Set 3 for strong turbulence.

Although the initial amount of entanglement is the same for all the Bell states, the subsequent evolution of the three sets are different. Hence, the initial amount of entanglement does not determine the evolution of the entanglement, as was found for the two-dimensional situation [27]. The Bell states of Set 3 maintain a nonzero entanglement for longer than the states of Set 1 and 2. This can be understood by considering the diagram in Fig. 11. The basis states that are used to compose the states in Set 1 ($|1,1\rangle, |0,0\rangle$ or $|-1,-1\rangle, |0,0\rangle$) have as their nearest neighbour basis states ($|1,0\rangle, |0,1\rangle$ or $|-1,0\rangle, |0,-1\rangle$) that can be combined with the original basis states to form separable states. The same situation is true for the states in Set 2. On the other hand, the nearest neighbour basis states for the states in Set 3 can not be combined with the original basis states in Set 3 to form separable states. Hence, one can argue that states from Set 3 have a slower entanglement decay than states from Set 1 and Set 2. This is confirmed by the difference in slope of the curve for Set 3 leaving the point at $t = 0$ compared to those of Sets 1 and 2.

9. Initially maximally entangled states

The maximally entangled qutrit states are divided into two groups according to the curves of the decay of their entanglement. Examples of these two groups are given by

$$\text{State 1} = \frac{1}{\sqrt{3}}\left[|1,1\rangle + |-1,-1\rangle + \exp\left(\mathrm{i}\phi_3\right)|0,0\rangle\right] \tag{97}$$

$$\text{State 2} = \frac{1}{\sqrt{3}}\left[|0,-1\rangle + |-1,0\rangle + |1,1\rangle\right], \tag{98}$$

respectively.

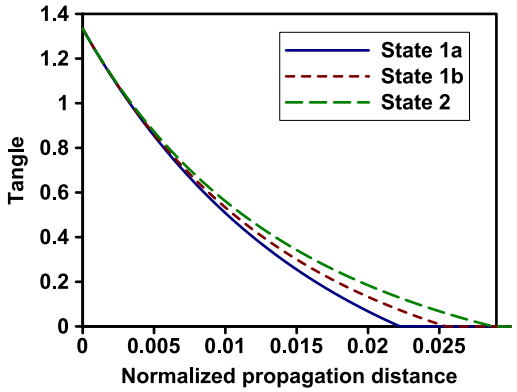

FIG. 14: Tangle evolution of the initially maximally entangled state in strong turbulence, showing three curves: State 1a, State 1b and State 2. State 1a and State 1b are obtained for $\phi = \pi$ and $\phi = 0$, respectively.

The only phase that affects the entanglement evolution in these states is the relative phase between the first two terms and the last term in State 1, as denoted by ϕ_3. We ignore all the other phases in these states. The optimal value of the phase ϕ_3, as a function of the propagation distance t_0 where the entanglement is maximized, is given by

$$\phi_3 = \phi_{\text{opt}}\left(t_0\right) = \arctan\left[\frac{2\ H_{\text{r}}(t_0)\ H_{\text{i}}(t_0)}{H_{\text{i}}(t_0)^2 - H_{\text{r}}(t_0)^2}\right], \tag{99}$$

where the functions $H_{\text{r}}(t)$ and $H_{\text{i}}(t)$ are given in Eqs. (89) and (90). We'll denote the cases with minimum and maximum tangle due to this phase as State 1a and State 1b, respectively.

The decay curves of State 1a, State 1b and State 2 are shown in Fig. 14, both in weak and strong turbulence. One finds that states represented by State 2 are more robust than those represented by State 1. At first the entanglement decay for all states is nearly identical and only starts to deviate as the entanglement decreases.

10. Robust entangled state

To find the robust states we start by performing numerical optimization of the tangle at a particular point $t = t_0$, for the most general initial pure state Eq. (91), using the parameterization from Eq. (93). This optimization

process is similarly to that in [32]. From the optimization results, we found that the robust states tend to have certain forms, given by

$$|\mu_1\rangle = \cos(\mu_1)\frac{1}{\sqrt{2}}\left[|1,1\rangle + |-1,-1\rangle\right] + \sin(\mu_1)\exp(\mathrm{i}\phi_3)\,|0,0\rangle \tag{100}$$

$$|\mu_2\rangle = \cos(\mu_2)\frac{1}{\sqrt{2}}\left[|0,-1\rangle + |-1,0\rangle\right] + \sin(\mu_2)\,|1,1\rangle\,, \tag{101}$$

where μ_1 and μ_2 represent the optimization angular parameters for the two states, respectively.

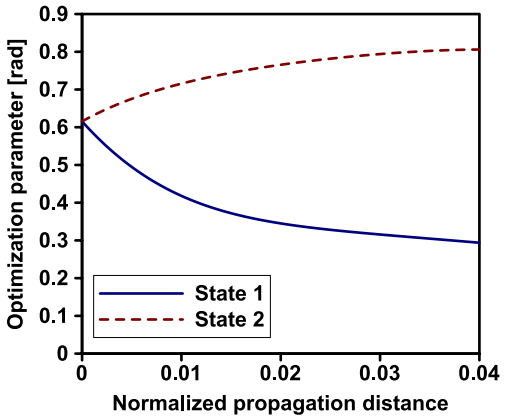

FIG. 15: Curves of optimized parameters $\mu_1(t_0)$ for State 1 and $\mu_2(t_0)$ for State 2 that gives the robust entangled states $|\mu_1\rangle$ and $|\mu_2\rangle$ as a function of the normalized propagation distance t_0 where optimization is done, in strong turbulence (a) and weak turbulence (b).

Optimizing μ_1 and μ_2 for maximal entanglement at $t = t_0$, we obtain the curves for the optimized parameters $\mu_1(t_0)$ and $\mu_2(t_0)$ shown in Fig. 15. The fact that the parameters are not independent of t_0 means that there does not exist one single state that is the robust state for all propagation distances. For $t_0 = 0$ the optimized states $|\mu_1(0)\rangle$ and $|\mu_2(0)\rangle$ are the maximally entangled states given in Eqs. (97) and (98), respectively, as expected.

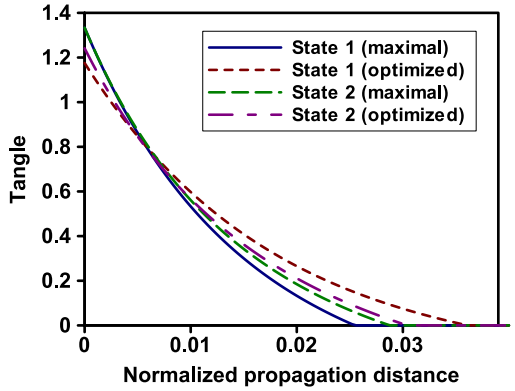

FIG. 16: Comparison of the tangle evolution of initially maximally entangled states (State 1 and State 2) to those of the optimized states $|\mu_1\rangle$ and $|\mu_2\rangle$, optimized at $t_0 = 0.03$.

Substituting (99) and the optimal values for μ_1 and μ_2 into (100) and (101), we obtain states that maintain a nonzero entanglement much longer than the initially maximally entangled states of (97) and (98) or the Bell states in (94), (95) and (96). The corresponding curves of the tangle are shown in Fig. 16.

11. Experimental preparation of robust states

The optimized state $|\mu_1\rangle$ has an additional benefit. All its terms have the same net OAM (=0). Therefore, it can be prepared experimentally in spontaneous parametric down-conversion (SPDC). The down-converted

states produced in SPDC have different weights for different OAM basis states [33, 34]. Moreover, this OAM spectrum can be changed (made broader or narrower) by adjusting the appropriate parameters (e.g. beam sizes) in the experiment. In this way one can control the value of μ_1. In case the range of weights that are thus produced does not include that which is required for the robust state, one can introduce mode sorting [35] — an interferometer that can separate the OAM modes according to their OAM indices — to separate the different modes so that they can be given different weights and phases (such as ϕ_3) before being recombined to form the required initial state. It would be harder to produce the optimized state $|\mu_2\rangle$, because the terms in this state do not have the same net OAM and would therefore not be directly produced in an SPDC process. However, using mode sorting [35] one can change the OAM and the weights in the individual terms of some state that can be obtained from SPDC, such that the result is the required optimized state $|\mu_2\rangle$.

VI. NUMERICAL SIMULATIONS

1. Motivation

   To know whether the theories about the decay of OAM entanglement in turbulence are correct, we need to compare it with some other results that were obtained independently, such as experimental results and numerical simulations. Here we discuss the numerical simulations.

   Using numerical simulations, one can avoid the challenges posed by the practical issues associated with quantum states in turbulence. Moreover, one can produce results that are independent of the theory and closer to the real thing. Numerical simulations are therefore an important intermediate effort between theory and experiment. If the theory, the numerical simulation results and the experimental results all agree, then one gains confidence that some understanding about the process has been achieved.

2. General procedure

   The numerical simulation of the propagation of an entangled bipartite quantum state through atmospheric turbulence is performed according to the following general procedure:

   - First one prepares an input states, consisting of a collection of different complex-valued functions (transverse spatial modes) that are pairwise associated with the two photons.
   - Next the different modes are propagated through the turbulent atmosphere. Here we use a split-step method that alternates between multiplying the mode with a random phase function and propagating the modulated result over a short distance of free-space (without turbulent). These two steps are performed repeatedly until one reached the final distance.
   - For each step one extracts the density matrix of the quantum states. From the sequence of density matrices thus obtained one can compute a curve of the entanglement as a function of the propagation distance.

   Each of these steps are discussed in more detail below.

3. Input state

   The input state can be any photonic quantum state that is entangled in terms of its spatial degrees of freedom. Consider for example the Bell state

   $$|\Psi\rangle = \frac{1}{\sqrt{2}} \left(|1\rangle_A |-1\rangle_B + |-1\rangle_A |1\rangle_B \right). \tag{102}$$

   Here $|1\rangle$ ($|-1\rangle$) represents an LG mode, given by Eq. (53), at the waist ($t = 0$) with $p = 0$ and $\ell = 1$ ($\ell = -1$). For example, $|1\rangle$ is associated with transverse spatial mode

   $$U_{01}^{(LG)} = 2\sqrt{\pi} r \exp(\mathrm{i}\phi) L_0^1(2r^2) \exp(-r^2), \tag{103}$$

   where $r = \sqrt{x^2 + y^2}/w_0$.

   For the duration of the simulation each of the four transverse modes, represented in Eq. (102), is propagated independently through the turbulence. Two of these modes are associated with the photon of subsystem-A and the other two with the photon of subsystem-B. The two photons propagate through different regions of the turbulent atmosphere. Therefore, the random phase screens for the two subsystems are different, but the two modes associated with the same photon are modulated by the same random phase screens.

4. Split-step method

The expression for the paraxial wave equation in a turbulent medium, as given in Eq. (38), can also be expressed as

$$\partial_z g(\mathbf{x}) = \frac{-i}{2k_0}\nabla_T^2 g(\mathbf{x}) - ik_0\delta n(\mathbf{x})g(\mathbf{x}). \tag{104}$$

The two terms on the right-hand side represent, respectively, the free-space propagation process and the modulation of the field by a random phase. The split-step method separates these two processes and performs them in consecutive steps. First the transverse optical field is modulated by the random phase, as if the optical beam passes through a thin phase screen. The random phase that is condensed into this phase screen represents that accumulated phase modulation that the optical field would have acquired after propagating through a turbulent medium for a distance Δz. The modulated optical field is then propagated through free-space without turbulence over a distance of Δz. After the free-space propagation the resulting optical field is modulated by the next random phase for the next Δz and then propagated through free-space again. This is repeated over and over again (N times) until a distance of $L(= N\Delta z)$ is reached where the entanglement has decayed to zero.

5. Random phase screens

The random phase screens are calculated in such a way as to produce the same effect that a turbulent atmosphere would produce. This is done by assuming that the turbulence can be modeled by the Kolmogorov theory. Therefore, the phase functions must reproduce the Kolmogorov structure function. For this purpose we model the phase of the transmission function of the phase screen by

$$\begin{aligned}\theta(x,y) &= \frac{k_0}{\Delta_k}\sqrt{\frac{\Delta z}{2\pi}}\int \tilde{\chi}_n(\mathbf{K})\left[\Phi_0(\mathbf{K},0)\right]^{1/2}\exp\left[-i(k_x x + k_y y)\right]\,\frac{\mathrm{d}^2k}{(2\pi)^2}\\ &= \frac{k_0}{\Delta_k}\sqrt{\frac{\Delta z}{2\pi}}\mathcal{F}^{-1}\left\{\tilde{\chi}_n(\mathbf{K})\left[\Phi_0(\mathbf{K},0)\right]^{1/2}\right\},\end{aligned} \tag{105}$$

where $\Phi_0(\mathbf{K},0)$ is the Kolmogorov power spectral density, with $k_z = 0$, $\tilde{\chi}(\mathbf{K})$ is a normally distributed two-dimensional random complex spectral function and Δ_k is its sample spacing in frequency domain. The latter is inversely proportional to the outer scale of the turbulence. Since the phase is an asymmetric real-valued function, we have that $\tilde{\chi}^*(\mathbf{K}) = \tilde{\chi}(-\mathbf{K})$.[d] Furthermore, the autocorrelation function of the random function is given by

$$\langle\tilde{\chi}(\mathbf{K}_1)\tilde{\chi}^*(\mathbf{K}_2)\rangle = (2\pi\Delta_k)^2\,\delta_2(\mathbf{K}_1 - \mathbf{K}_2). \tag{106}$$

An example of such a random phase function is shown in Fig. 17.

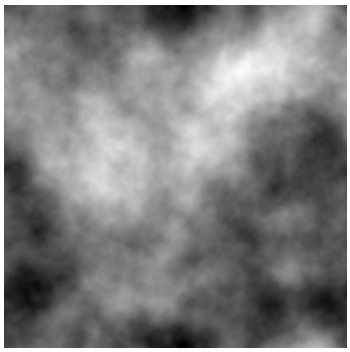

FIG. 17: Example of the phase of a random phase screen. The gray scales represent the phase values.

One can determine whether the phase thus produced represents Kolmogorov turbulence, by testing to see if it reproduces the phase structure function, given by Eq. (30), when substituted into Eq. (2). It turns out that

[d] In practice this restriction is dropped, leading to a complex function for the phase, which then represents two distinct phase functions that can be used for two phase screens.

if the phase function in Eq. (105) is produced by a discreet inverse Fourier transform, such as the fast Fourier transform algorithm, then the result from Eq. (2) does not give the structure function in Eq. (30). The reason is that the Kolmogorov power spectral density function is sharply peak at the origin, as shown in Fig. 3. Moreover, the value at the origin of the spectrum is singular. So the discreet sample at the origin is usually discarded and the rest of the samples are insignificant because the bulk of the power in the spectrum sits between the sample at the origin and the first neigbouring samples. Additional samples need to be added between the sample at the origin and the first neigbouring samples. This can be done by adding subgrids with smaller sample spacings in this region, as shown in Fig. 18. With enough extra samples in such subgrids the resulting phase function reproduces the structure function in Eq. (30) accurately.

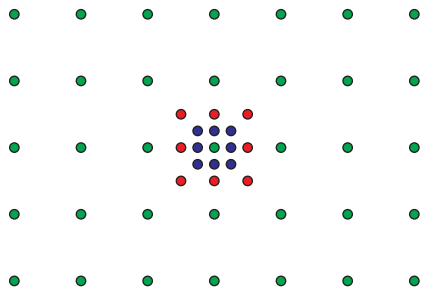

FIG. 18: Diagram of the grid points on the Fourier domain. The original grid points are shown as green dots. The red and blue dots are progressively smaller subgrids around the origin.

6. Extracting the density matrix

The physical process that a quantum state experiences while propagating through a particular turbulent medium is unitary. Therefore, the distorted state is still a pure state. However, we do not know the details of the medium that the quantum state propagated through. We can only make predictions based on the statistical properties of the medium. Therefore, we need to compute an ensemble average of the results over all the possible turbulent media that have these particular statistical properties. The result is a mixed state.

We need to do the same in the numerical simulation. The modes that represent the different components of the input state become distorted in the numerical simulation due to the repeated phase modulations and propagations. However, together they still represent a pure quantum state. If $U_{\Delta z}$ represents the unitary operation for the propagation through a particular turbulent medium of thickness Δz, then the simulation implements the operation

$$\sum_n \alpha_n \left|\psi_n\right\rangle_A \left|\psi_n\right\rangle_B \to \sum_n \alpha_n \left(U_{\Delta z} \left|\psi_n\right\rangle_A\right) \left(U_{\Delta z} \left|\psi_n\right\rangle_B\right). \tag{107}$$

For the qubit case under consideration, the distortions are represented by

$$\left|\pm 1\right\rangle_X \to a_{\pm 1,X} \left|1\right\rangle_X + b_{\pm 1,X} \left|-1\right\rangle_X, \tag{108}$$

for the respective subsystems, where X is either A or B and the coefficients are given by inner products

$$\begin{aligned} a_{\pm 1,X} &= \left\langle \pm 1\right| U_{\Delta z} \left|1\right\rangle_X \\ b_{\pm 1,X} &= \left\langle \pm 1\right| U_{\Delta z} \left|-1\right\rangle_X. \end{aligned} \tag{109}$$

For a particular sequence of random phase screens the initial state transforms to

$$\left|\Psi_{\text{in}}\right\rangle \to \left|\Psi_{\text{out}}\right\rangle = C_1 \left|1\right\rangle_A \left|1\right\rangle_B + C_2 \left|1\right\rangle_A \left|-1\right\rangle_B + C_3 \left|-1\right\rangle_A \left|1\right\rangle_B + C_4 \left|-1\right\rangle_A \left|-1\right\rangle_B, \tag{110}$$

where

$$\begin{aligned} C_1 &= \frac{1}{\sqrt{2}} \left(a_{1,A} a_{-1,B} + a_{-1,A} a_{1,B}\right) \\ C_2 &= \frac{1}{\sqrt{2}} \left(a_{1,A} b_{-1,B} + a_{-1,A} b_{1,B}\right) \\ C_3 &= \frac{1}{\sqrt{2}} \left(b_{1,A} a_{-1,B} + b_{-1,A} a_{1,B}\right) \\ C_4 &= \frac{1}{\sqrt{2}} \left(b_{1,A} b_{-1,B} + b_{-1,A} b_{1,B}\right). \end{aligned} \tag{111}$$

Note that only a restricted set of basis elements are retained. As a result the transformation in Eq. (110) is not unitary ($|\Psi_{\text{out}}\rangle \neq U_{\Delta z}|\Psi_{\text{in}}\rangle$). The implied truncation represents a post-selection process, leading to a density matrix with a reduced trace. Therefore, the density matrix needs to be normalized. The final density matrix is calculated by

$$\rho = \frac{\sum_n^N |\Psi_n\rangle\langle\Psi_n|}{\text{Tr}\left\{\sum_n^N |\Psi_n\rangle\langle\Psi_n|\right\}}, \tag{112}$$

for N different instances of the medium (different sequences of random phase screens), where $|\Psi_n\rangle$ is the n-th state obtained from the transformation in Eq. (110).

The resulting density matrix is used to compute the concurrence, or any other quantity of interest.

7. Results

The results from the numerical simulations are presented together with the experimental results below.

VII. EXPERIMENTAL RESULTS

1. Coincidence counts

The first experimental work studying quantum photonic states in turbulence was done by Pors, *et al.* [36]. They looked at the effect that turbulence has on the coincidence counts as a function of the angular difference between two angular sectored phase plates. They used the results to relate the Shannon dimensionality, which gives the effective number of modes that can be detected, to the density operator of the measured state.

2. Power coupled into neigbouring OAM modes

Following the work in [19], Rodenburg, *et al.* [37] performed experimental measurements of the power coupled into neigbouring OAM modes, where the turbulence is simulated by a random phase on a spatial light modulator. They found results that agreed fairly well with the theoretical calculation in [19]. Subsequently these results were used to propose the use of plane waves instead of OAM modes to encode quantum information [38–40].

3. Channel capacity

The work on OAM states in turbulence is ultimately relevant for the implementation of free-space quantum communication. Such a technology require the successful implementation of quantum protocols for quantum key distribution, using OAM photonic states. To see if this is feasible, Malik, *et al.* [41], measured the channel capacity experimentally through turbulence, simulated by a single phase screen. The results were obtained over a range of values for D/r_0, where D is the size of the receiving aperture and r_0 is the Fried parameter, Eq. (31). Their results show that for larger sets of OAM modes one can increases the number of bits per photon beyond what is possible with qubits. However, at $D/r_0 \sim 1$ this channel capacity starts to decay to zero. Zhao, *et al.* [42] also measured the channel capacity experimentally through turbulence, but they also incorporated aberration correction and showed that they can improve the performance of the system to some extent.

4. Entanglement

Although the channel capacity and other such quantities are relevant for the physical implementation of a practical quantum communication system, they don't say much about whether the quantum state retained its entanglement. To determine the extent to which a quantum state retains its initial entanglement one needs to measure the entanglement of the state. Although there are special circumstances where one can measure the entanglement directly [38], these circumstances do not apply when we consider the state in terms of the OAM modes. Therefore, one needs to perform a full quantum state tomography to determine the density matrix of the state and then one can compute the entanglement of the density matrix using the concurrence or some other quantitative measure of the entanglement.

5. Preparation of the entangled state (SPDC)

A pair of photons that is entangled in its spatial degrees of freedom, is readily produced through spontaneous parametric down-conversion (SPDC). An experimental setup that produces such an entangled state is shown by the diagram in Fig. 19. In the diagram a 350 mW laser with a wavelength of 355 nm is used to pump a 0.5 mm-thick BBO crystal with type I phase-matching, to produce collinear, degenerate photon pairs. The signal

and idler photons are separated by a 50/50 beam splitter. The resulting OAM entangled quantum state is now sent through a dissipative channel that represents atmospheric turbulence. In the experiment the turbulence is simulated by a single phase screen, which is implemented through phase modulation by spatial light modulators (SLMs). The quantum state that is obtained after the dissipative channel is then measured with full quantum state tomography. In the practical experiment the SLMs that simulate the dissipative channel are also used for the quantum state tomography. The crystal plane is imaged onto the two SLMs in the signal and idler beams, respectively, and the SLM planes are imaged onto the entrance pupils of single-mode fibers (SMFs), which extract the pure Gaussian mode from the incident field. Avalanche photo diodes (APDs), connected to the other ends of these SMFs, register photon pairs via a coincidence counter (CC).

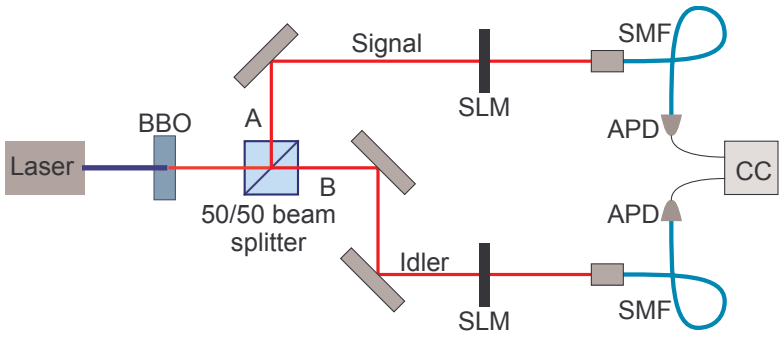

FIG. 19: Diagram of the experimental setup used to measure the amount of entanglement that survives after a certain amount of scintillation caused by simulated turbulence.

6. Distorted modes

One way to look at the effect of the simulated turbulence on the OAM basis states in the experiment is to do a back-projection: one of the APDs is replaced by a laser diode, which then sends light backward from the SMF, illuminating the SLM that contains the random phase of the turbulence as well as the phase of the OAM mode to be detected. One can now image this light coming from the SLM to see the effect of the scintillation, as shown in Fig. 20. We see that the modes become progressively more distorted due to the scintillation.

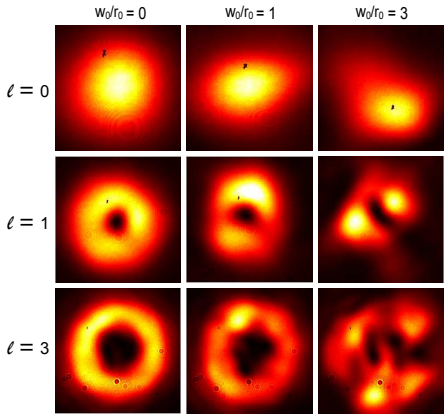

FIG. 20: Intensity profiles of different OAM modes ($\ell = 0, 1, 3$), produced by back-projection from the SMF, for different amounts of scintillation ($w_0/r_0 = 0, 1, 3$).

7. Modal scattering

The quantum state produced by the SPDC process is entangled in terms of the OAM modes, so that the sum of the azimuthal indices of the signal and idler beams gives the azimuthal index of the pump. If the pump has $\ell = 0$, as we have in this experiment, the azimuthal indices of the signal and idler beams are anticorrelated $\ell_{\text{signal}} = -\ell_{\text{idler}}$. When there is no turbulence, one observes an anticorrelated diagonal in the diagram of coincidence counts for the different combinations of azimuthal indices, as can be observed in Fig. 21(a) and (d).

In the presence of turbulence, the OAM modes in each of the beams are scattered to other OAM modes. This produces the off-diagonal coincidence counts observed in Fig. 21(b), (c), (e) and (f).

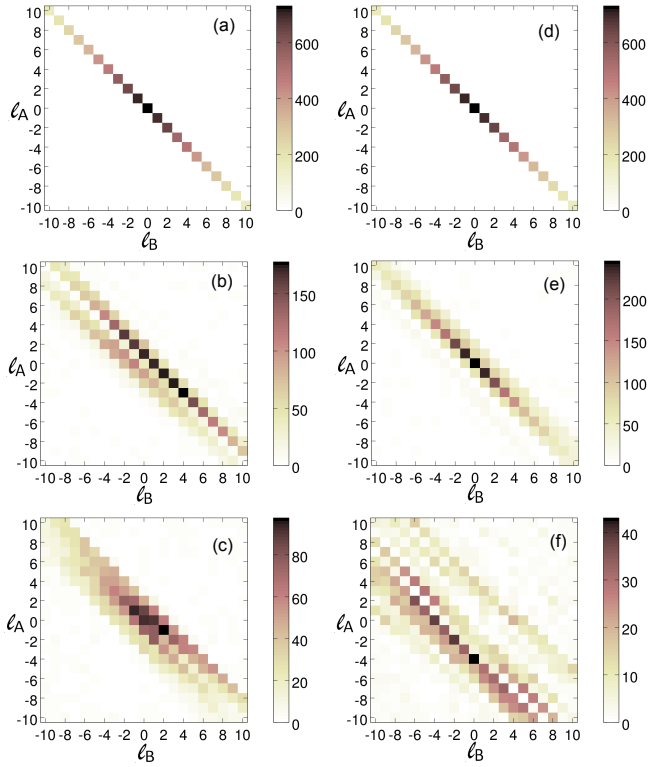

FIG. 21: Diagram showing the coincidence counts for simultaneous measurements of modes with azimuthal index ℓ_A in the signal beam and ℓ_B in the idler beam when one or both beams passed through turbulence. In (a), (b) and (c) only one photon passed through turbulence and in (d),(e) and (f) both photons passed through turbulence. In (a) and (d) the turbulence is zero. In (b) and (e) the turbulence produces a scintillation of $w_0/r_0 = 2$, and in (c) and (f) it produces a scintillation of $w_0/r_0 = 4$.

8. Comparison of results

The experimental results are compared to the results from numerical simulations and to the predictions from the single phase screen calculations and from the IPE. These results are shown for the following cases. In Fig. 22 only one photon propagated through turbulence. Four graphs are shown for $\ell = 1, 3, 5, 7$, respectively. Each graph is shown as a function of the scintillation strength, as quantified by w_0/r_0, up to a value of $w_0/r_0 = 4$. The results in Fig. 23 is the equivalent for the case where both photons propagate through turbulence.

In general the experimental results and the numerical simulations agree fairly well with the predictions of the single phase screen calculations, but the IPE predictions are only in agreement with the other results in the case where $\ell = 1$. As explained above, the reason is that the IPE is severely sensitive to truncations of the density matrix.

9. Distance scale for entanglement decay

All the results on the decay of OAM entanglement in turbulence points to the fact that the entanglement decays where w_0/r_0 is on the order of 1. This implies that the nominal distance scale at which atmospherically induced decay of entanglement occurs is given by

$$L_{\text{dec}} \sim \frac{0.06\lambda^2}{w_0^{5/3} C_n^2}. \tag{113}$$

One can argue that this scale should also depend on the azimuthal index ℓ. To find this ℓ-dependence, we use the single phase screen calculations to find the values of w_0/r_0 where the concurrence is equal to 0.5 over a range of ℓ-values. These values show that a power law governs the ℓ-dependence of L_{dec}. The resulting expression for

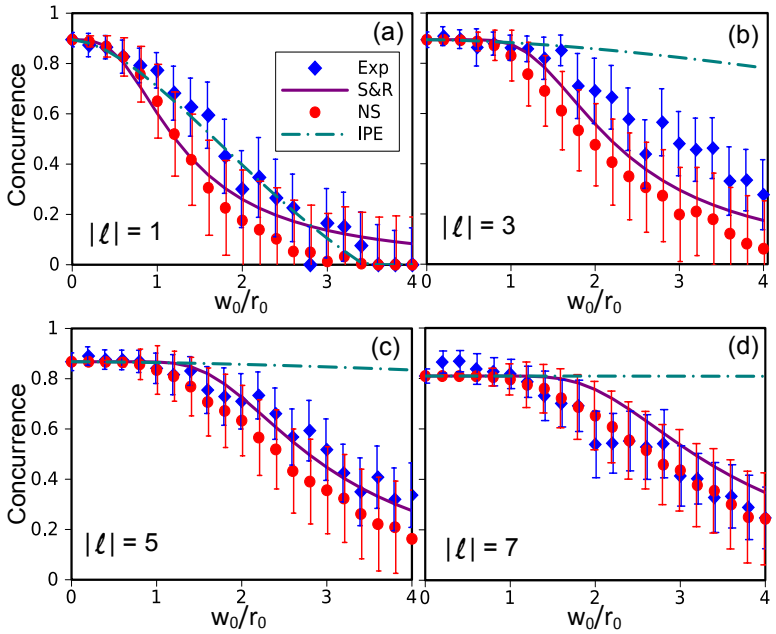

FIG. 22: Comparison of experimental measurements (red dots), numerical simulations (blue diamonds), single phase screen predictions (maroon line) and IPE predictions (turquoise dot-dashed line) for the case where only one photon passes through turbulence. The graphs in (a), (b), (c) and (d), respectively show the results for $\ell = 1, 3, 5, 7$.

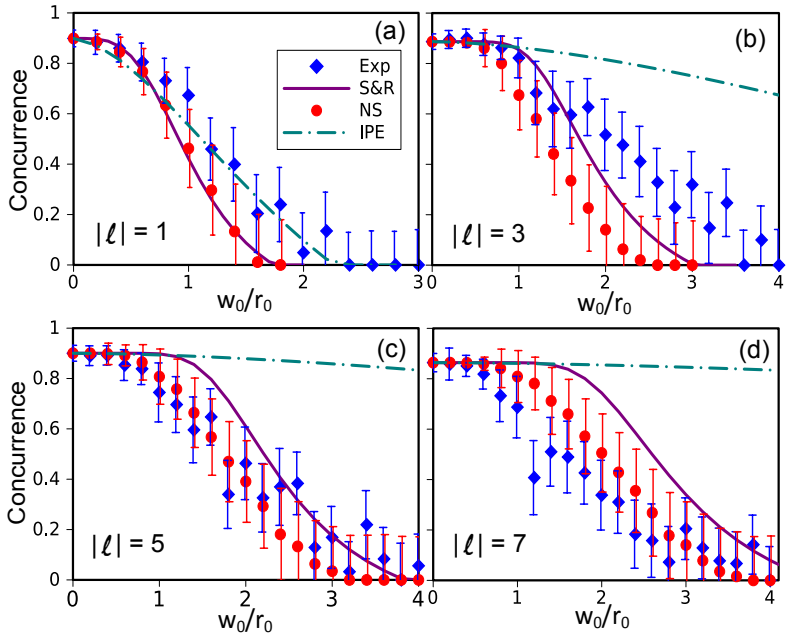

FIG. 23: Comparison of experimental measurements (red dots), numerical simulations (blue diamonds), single phase screen predictions (maroon line) and IPE predictions (turquoise dot-dashed line) for the case where both photons pass through turbulence. The graphs in (a), (b), (c) and (d), respectively show the results for $\ell = 1, 3, 5, 7$.

the distance scale where atmospherically induced decay of entanglement occurs is

$$L_{\text{dec}}(\ell) = \frac{0.06\lambda^2\sqrt{\ell}}{w_0^{5/3}C_n^2}. \tag{114}$$

[1] L. C. Andrews and R. L. Phillips, *Laser Beam Propagation Through Random Media* (SPIE, Washington, 1998).
[2] A. Papoulis, *The Fourier integral and its applications*, McGraw-Hill electronic sciences series (McGraw-Hill, 1962).
[3] A. Aspect, P. Grangier, and G. Roger, Phys. Rev. Lett. **47**, 460 (1981).
[4] J. S. Bell, Physics (N.Y.) **1**, 195 (1965).
[5] S. Hill and W. K. Wootters, Phys. Rev. Lett. **78**, 5022 (1997).
[6] W. K. Wootters, Phys. Rev. Lett. **80**, 2245 (1998).
[7] C. Paterson, Phys. Rev. Lett. **94**, 153901 (2005).
[8] B. J. Smith and M. G. Raymer, Phys. Rev. A **74**, 062104 (2006).
[9] C. Gopaul and R. Andrews, New Journal of Physics **9**, 94 (2007).
[10] A. A. Semenov and W. Vogel, Phys. Rev. A **80**, 021802 (2009).
[11] A. K. Jha, G. A. Tyler, and R. W. Boyd, Phys. Rev. A **81**, 053832 (2010).
[12] M. A. Nielsen and I. L. Chuang, *Quantum computation and quantum information* (Cambridge university press, 2010).
[13] D. L. Fried, J. Opt. Soc. Am. **56**, 1372 (1966).
[14] D. L. Fried, J. Opt. Soc. Am. A **15**, 2759 (1998).
[15] G. Gbur and R. K. Tyson, J. Opt. Soc. Am. A **25**, 225 (2008).
[16] A. Dipankar, R. Marchiano, and P. Sagaut, Phys. Rev. E **80**, 046609 (2009).
[17] V. V. Voitsekhovich, D. Kouznetsov, and D. K. Morozov, Appl. Opt. **37**, 4525 (1998).
[18] R. Rao, Appl. Opt. **47**, 269 (2008).
[19] G. Tyler and R. Boyd, Opt. Lett. **34**, 142 (2009).
[20] A. A. Semenov and W. Vogel, Phys. Rev. A **81**, 023835 (2010).
[21] F. S. Roux, Phys. Rev. A **83**, 053822 (2011).
[22] F. S. Roux, arXiv preprint arXiv:1110.3593 (2011).
[23] T. Brünner and F. S. Roux, New J. Phys. **15**, 063005 (2013).
[24] M. Abramowitz and I. A. Stegun, *Handbook of Mathematical Functions* (Dover, Toronto, 1972).
[25] E. Barnes, Proc. London Math. Soc. **s2-6**, 141177 (1908).
[26] F. Mintert and A. Buchleitner, Phys. Rev. Lett. **98**, 140505 (2007).
[27] T. Konrad, F. de Melo, M. Tiersch, C. Kasztelan, A. Aragão, and A. Buchleitner, Nature Physics **4**, 99 (2007).
[28] M. Tiersch, F. de Melo, and A. Buchleitner, Phys. Rev. Lett. **101**, 170502 (2008).
[29] M. Tiersch, F. de Melo, T. Konrad, and A. Buchleitner, Quantum Information Processing **8**, 523 (2009).
[30] G. Gour, Phys. Rev. Lett. **105**, 190504 (2010).
[31] V. Gheorghiu and G. Gour, arXiv preprint arXiv:1205.2667 (2012).
[32] F. Mintert, J. Phys. A: Math. Gen. **43**, 245303 (2010).
[33] J. P. Torres, A. Alexandrescu, and L. Torner, Phys. Rev. A **68**, 050301 (2003).
[34] F. M. Miatto, A. M. Yao, and S. M. Barnett, Phys. Rev. A **83**, 033816 (2011).
[35] J. Leach, M. J. Padgett, S. M. Barnett, S. Franke-Arnold, and J. Courtial, Phys. Rev. Lett. **88**, 257901 (2002).
[36] B.-J. Pors, C. H. Monken, E. R. Eliel, and J. P. Woerdman, Opt. Express **19**, 6671 (2011).
[37] B. Rodenburg, M. P. Lavery, M. Malik, M. N. OSullivan, M. Mirhosseini, D. J. Robertson, M. Padgett, and R. W. Boyd, Opt. Lett. **37**, 3735 (2012).
[38] A. K. Jha and R. W. Boyd, Phys. Rev. A **81**, 013828 (2010).
[39] R. W. Boyd, B. Rodenburg, M. Mirhosseini, and S. M. Barnett, Opt. Express **19**, 18310 (2011).
[40] M. Mirhosseini, B. Rodenburg, M. Malik, and R. W. Boyd, arXiv preprint arXiv:1304.0709 (2013).
[41] M. Malik, M. O'Sullivan, B. Rodenburg, M. Mirhosseini, J. Leach, M. P. J. Lavery, M. J. Padgett, and R. W. Boyd, Opt. Express **20**, 13195 (2012).
[42] S. M. Zhao, J. Leach, L. Y. Gong, J. Ding, and B. Y. Zheng, Opt. Express **20**, 452 (2012).